Control of Very Lightweight 2-DOF Single-Link Flexible Robots Robust to Strain Gauge Sensor Disturbances: A Fractional-Order Approach

Daniel Feliu-Talegon and Vicente Feliu-Batlle, *Senior Member, IEEE*

***Abstract*— This article deals with the control of two degrees of freedom manipulators that have a flexible and very lightweight link. These robots have a single low-frequency and high-amplitude vibration mode. Their actuators have high friction, and their vibration sensors are often strain gauges that have offset and high-frequency noise. These problems reduce the robot precision and produce noisy control signals that saturate actuators. An efficient control system is proposed to overcome these drawbacks. Actuator friction effect is nearly removed by closing a high gain position control loop around the actuator. It causes the separation of the robot dynamics into the controlled actuator fast subsystem and the link dynamics slow subsystem. Based on that, an innovative control system is designed to remove vibrations using the singular perturbation theory combined with the input-state linearization technique. This control system includes fractional-order controllers that nearly remove unknown sensor offset and sensor ramp disturbances while reducing the high-frequency component of the control signal caused by sensor noise. Simulated and experimental results show the superior performance of these controllers over other standard integer-order controllers of similar complexity and nominal behavior.**

***Index Terms*— Control of vibrations, flexible robots, fractional-order controller, high-frequency noise.**

I. Introduction

SOME robotic applications demand lighter and larger robots that can be driven using smaller amounts of energy and can be more easily transported. Unfortunately, the flexibility of the links of these robots produces oscillations during motion that make the precise positioning of their tips extremely difficult.

Though a flexible link robot has infinite vibration modes, only a small number of them is usually considered in the design of its control system. This number depends on the ratio between the links and the payload masses: the lower this ratio, i.e., the lighter the links and the heavier the payload, the smaller the number of significant vibration modes.

Links made of composite materials (e.g., the graphite–epoxy of fiberglass) are able to carry heavy payloads in spite of being very lightweight. Robots with large thin links made of these materials, therefore, often have very small link-payload mass ratios that allow us to regard them as having a single vibration mode. This greatly simplifies the dynamic models of these robots and facilitates the design of their controllers. However, there are several technological problems in the implementation of these controls, which must be considered, and have not been satisfactorily solved yet, which are described in the following.

One problem is the significant Coulomb friction of the robot actuators, which is a discontinuous nonlinearity that makes difficult the precise positioning of the robot.

Another problem is the disturbances of the vibration sensors of flexible robots. These robots often use strain gauges because they allow measuring both vibrations and deflections and are cheap. However, strain gauges have several drawbacks: 1) they are prone to variations in temperature [1]; 2) they have high-frequency noise, due to electromagnetic interferences [2], which may cause saturation in the actuators, thus leading to bad dynamic performance, and may impede the accurate observation of the robot state (often needed for control) [3]; and 3) they have offset, which prompts a steady-state error in the closed-loop positioning of the links [4].

In particular, reducing offset is mandatory because it decreases the precision of the robot. This problem is normally overcome by executing a calibration process before the robot starts moving. However, the offset value may vary over time and a calibration process may, therefore, be required before the execution of each trajectory in order to remove the offset during that movement. This calibration may be more or less time consuming according to the positioning precision required. Besides being a waste of time, this process is sometimes ineffective as regards completely removing the offset because its value may vary throughout the movement. Devising control systems that remove the steady-state error caused by the offset is, therefore, of the utmost importance.

This article consequently studies the control of robots of several DOF (degrees of freedom) that have a particular mechanical configuration: one flexible link with azimuthal

Manuscript received September 22, 2020; revised December 24, 2020; accepted January 13, 2021. Date of publication February 3, 2021; date of current version December 15, 2021. Manuscript received in final form January 20, 2021. This work was supported in part by the Spanish Program under Grant FPU14/02256, in part by the Spanish State Research Agency, and in part by the European Social Fund (AEI/FEDER, UE) under Project PID2019-111278RB-C21. Recommended by Associate Editor S. Dadras. *(Corresponding author: Daniel Feliu-Talegon.)*

Daniel Feliu-Talegon is with the Robotics, Vision and Control Group, University of Seville, 41004 Seville, Spain (e-mail: danielfeliu91@hotmail.com).

Vicente Feliu-Batlle is with the E.T.S. Ingenieros Industriales, University of Castilla-La Mancha, 13071 Ciudad Real, Spain, and also with the Instituto de Investigaciones Energéticas y Aplicaciones Industriales, University of Castilla-La Mancha, 13071 Ciudad Real, Spain (e-mail: vicente.feliu@uclm.es).

Color versions of one or more figures in this article are available at https://doi.org/10.1109/TCST.2021.3053857.

Digital Object Identifier 10.1109/TCST.2021.3053857

and attitude degrees of freedom (2-DOF-1FL robots), whose parameters are known with the exception of the friction of the actuators and the disturbances of the strain gauge sensor.

This article is organized as follows. Section II presents the proposed control approach and justifies its contribution with respect to previous works. Section III describes the dynamics of our robot. Section IV develops the proposed control structure. Section V studies the conditions required to achieve robustness to strain gauge disturbances and presents the design of using a fractional-order controller (FOC). Section VI applies the previous results to the fast and accurate control of a flexible link sensing antenna and shows that an FOC is superior to other equivalent integer-order controllers (IOCs). Finally, some conclusions are given in Section VII.

II. Contributions and Related Work

The contributions are the following: 1) an innovative control system based on two nested loops that remove vibrations and minimize actuator friction effects; 2) controllers that significantly improve the precision of the robot tip positioning by reducing the effect of the offset and noise of strain gauge sensors; and 3) an improvement to the results attained in 2) by using an FOC rather than an equivalent IOC. These contributions are put into context in Section II-A.

A. Control System

Since the dynamics of our robots is nonlinear and most parameters are known, the input-state feedback linearization technique (see [5]) is used to design their controllers. Single-link flexible robots were controlled with this technique in [6] and, subsequently, robots with two flexible links [7].

A drawback of the above technique is that the Coulomb friction of the actuators may introduce undesirable steady-state errors. These can be removed by introducing an integral term in the controller at the cost of reducing the stability robustness (which can be a critical issue in robots, whose payload changes) [8]. Another solution is to use a two nested loop control scheme [9] that will be described in Section III.

The two nested loop control scheme allows us to divide the system into two simpler subsystems and subsequently use the input-state feedback linearization technique to control the slow subsystem and the singular perturbation theory to guarantee the complete stability of the system.

The singular perturbation theory has been used with single-link [10] and multilink [11] flexible robots. It considers the rigid dynamics as the slow subsystem and the flexible dynamics as the fast subsystem. It has been applied using different control techniques, such as composite learning combined with sliding mode control [12] or neural networks plus disturbance observers [13]. However, robots of very low stiffness—as is our case—may not accurately follow desired trajectories because the coupling between slow and fast subsystems cannot be neglected. This drawback and the fact that a high gain inner loop is closed in order to reduce the effect of actuator friction—which makes the rigid dynamics faster than the flexible link dynamics—make unsuitable the previous applications of the singular perturbation theory and motivate that this theory is applied differently in this article to that shown in previous research: the vibration mode of the link is considered to be the slow subsystem and the actuator dynamics the fast subsystem.

B. Robustness to Sensor Disturbances

High-pass filters are used to remove the offset of strain gauges. However, they eliminate the constant component caused by gravity, which is needed by the feedback controllers of robots in order to achieve a precise tip attitude positioning. These filters may be useful for movements on the horizontal plane or 3-D movements in outer space—where the action of gravity can be ignored—but they drastically reduce the position accuracy of a flexible link robot when gravity is present.

The aforementioned control methods, and others listed in [1], are sensitive to strain gauge disturbances. In particular, offset produces position steady errors. Artificial intelligence techniques have been applied to flexible link robots, such as fuzzy logic [14] or neural network [15] controllers. However, they have not proved to be robust to either actuator friction or sensor disturbances. A new method, therefore, is developed here to remove these disturbances.

C. FOC to Increase Robustness to Sensor Disturbances

FOCs have been already applied to industrial robots with rigid links [16]. However, their application to flexible robots is rare. The control of one horizontal degree of freedom single-link flexible robot (1-DOF-1FL robot) using strain gauges was addressed in [17]. Since that robot moved on a horizontal plane, it had a linear time-invariant dynamics. This article in question developed: 1) a control structure that reduced the tip position error caused by sensor offset and 2) a linear FOC (FOCs are described in [18]) embedded in that structure that attenuated the effect of sensor noise better than any equivalent IOC. We apply the control system from [17] to 2-DOF-1FL robots in order to take advantage of the robustness properties of its FOC. This application is not straightforward because these robots are nonlinear and have static deflection caused by gravity, unlike the robot in [17], which is linear and has no such deflection. Our new control system, therefore, involves the use of a nonlinear controller, the development of a nonlinear and multivariable version of the previous control structure robust to sensor offset, and an adaptation of the FOC from [17].

III. Dynamic Model

A. Link Dynamics

We assume links that have certain specific features.

1) The deflections of the points of the link are small when compared to their distance to the base. This is usually assumed when obtaining the dynamic models of flexible links [19].
2) Uniform link in Section I and elasticity coefficient E through the link.
3) Link of negligible mass, length l, and a rigidity constant $\kappa = 3EI/l$.
4) A tip payload that is a lumped mass of value m_t.

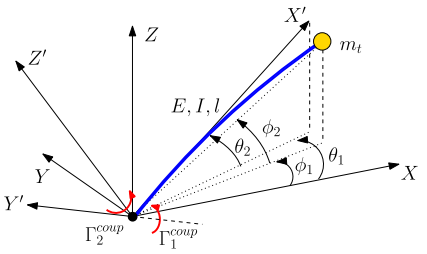

Fig. 1. Scheme of a 2-DOF single flexible link.

The dynamic model yielded by these hypotheses can also be used for a link whose mass is significantly lower than the tip payload mass. If it were also assumed that the payload does not have rotational inertia, only one vibration mode would be apparent. Moreover, if the link rotates on the horizontal plane, its dynamics can be accurately approximated by using a second-order linear system (see [20]).

Fig. 1 shows our 2-DOF-1FL robot. In this figure, joint angles are denoted as θ_i and tip angles as ϕ_i, whose subindexes $i = 1, 2$ represent azimuthal and attitude angles, respectively. Its dynamic model, assuming that the link verifies features 1)–4) and the payload has negligible rotational inertia, is then obtained from [21]

$$\begin{aligned} \dot{\hat{\boldsymbol{x}}} &= \begin{pmatrix} \hat{x}_3 \\ \hat{x}_4 \\ \mathbf{P}(\hat{\boldsymbol{x}}) + K_a \cdot \boldsymbol{\mu}(\boldsymbol{\theta},\ \boldsymbol{\phi}) \end{pmatrix} \\ \boldsymbol{\phi} &= \mathbf{C} \cdot \hat{\boldsymbol{x}} \end{aligned} \tag{1}$$

in which

$$\mathbf{P}(\hat{\boldsymbol{x}}) = \begin{pmatrix} 2 \cdot \tan(\hat{x}_2) \cdot \hat{x}_3 \cdot \hat{x}_4 \\ -K_g \cdot \cos(\hat{x}_2) - \sin(\hat{x}_2) \cdot \cos(\hat{x}_2) \cdot \hat{x}_3^2 \end{pmatrix} \tag{2}$$

$$\begin{aligned} \boldsymbol{\mu} &= \boldsymbol{\mu}(\boldsymbol{\theta},\ \boldsymbol{\phi}) \\ &= \begin{pmatrix} \sin(\theta_1 - \phi_1) \cdot \dfrac{\cos(\theta_2)}{\cos(\phi_2)} \\ \cos(\phi_2) \cdot \sin(\theta_2) - \cos(\theta_1 - \phi_1) \cdot \sin(\phi_2) \cdot \cos(\theta_2) \end{pmatrix} \end{aligned} \tag{3}$$

$$\mathbf{C} = (\mathbf{I}_2 \quad \mathbf{0}_{2,2}) \tag{4}$$

where $\boldsymbol{\theta} = (\theta_1\ \theta_2)^T$ is the input vector, $\boldsymbol{\phi} = (\phi_1\ \phi_2)^T$ is the output vector, $\hat{\boldsymbol{x}} = (\boldsymbol{\phi}^T\ \dot{\boldsymbol{\phi}}^T)^T$ is the state vector, the upper T signifies transpose, $K_g = g/l$, $K_a = \kappa/(m_t \cdot l^2)$, g is the gravity constant, $\mathbf{I}_k$ is the identity matrix of dimension $k \times k$, and $\mathbf{0}_{k,l}$ is the matrix of zeros of dimension $k \times l$.

Equation (1) describes a four-state nonlinear multivariable system whose outputs, ϕ_1 and ϕ_2, represent the spherical coordinates of the tip payload position.

The moment applied to the base of the link by the actuators or, equivalently, the coupling torque between the link and the set of actuators can be defined by its components in the directions of the azimuthal and attitude degrees of freedom Γ_1^{coup} and Γ_2^{coup}, respectively. These are given by

$$\begin{aligned} \Gamma_1^{\text{coup}} &= \kappa \cdot \sin(\theta_1 - \phi_1) \cos(\theta_2) \cos(\phi_2) \\ \Gamma_2^{\text{coup}} &= \kappa \cdot (-\cos(\theta_1 - \phi_1) \cos(\theta_2) \sin(\phi_2) \\ &\quad + \cos(\phi_2) \sin(\theta_2)). \end{aligned} \tag{5}$$

B. Actuator Dynamics

DC motors with high ratio reduction gears actuate our 2-DOF-1FL robots. The dynamic model of the motor is

$$\Gamma_i = n_i K_{mi} q_i = J_i \ddot{\theta}_i + \nu_i \dot{\theta}_i + \Gamma_i^{\text{nlc}} + \Gamma_i^{\text{coup}} \tag{6}$$

where the subindex $i = 1, 2$ is the azimuthal or attitude joint and n_i is the ratio of the reduction gear. In this equation, voltages q_i are the control signals. As it is assumed that the motors have servo amplifiers with very fast dynamics, the currents of the motors and, therefore, the motor torques Γ_i, are assumed to be proportional to the previous voltages. K_{mi} are the motor constants that define this proportionality, ν_i are the corresponding viscous friction coefficients, and J_i are the motor rotational inertias. Γ_i^{coup} are the moments transmitted by the actuators to the link and Γ_i^{nlc} are the Coulomb friction terms, which are nonlinear. In summary, the inputs to the system are voltages q_1 and q_2, which are applied to the motors, and the outputs are angles θ_1 and θ_2.

The complete dynamic model is, therefore, provided by (1)–(5), plus (6), which are particularized for the 2-DOF $i = 1, 2$. The complete system is, therefore, an eighth-order differential equation with two inputs, q_1 and q_2, and two outputs, ϕ_1 and ϕ_2. The Coulomb friction of the motors is considered disturbances.

IV. Control Scheme

A. General Description

Motor positions θ_i and moments at the base of the link Γ_i^{coup} are often used to control flexible links [22]. They are obtained using optical encoders and strain gauge bridges, which are placed at the base of the flexible links. Control laws often feedback the tip position of the flexible link, which is estimated by combining these measurements.

The strategy proposed in this work consists of dividing the control system into two nested loops (denominated as the inner and outer loops) such that the output of the control law of the outer loop is the reference of the inner loop. The inner loop is responsible for controlling the position of the actuators in such a way that the effects of nonlinear and time-varying frictions are almost removed. The outer loop is responsible for controlling the outputs of the system in such a way that vibrations are removed [9].

This methodology makes it possible to design the control system in two separate stages that have different objectives. First, the inner loop is designed to move the actuators as quick as possible without saturating the actuators. The usually more complex outer loop is then designed in order to achieve the desired behavior of the complete system. The complete closed-loop dynamics is subsequently integrated into a singularly perturbed model in order to assess the stability of the closed-loop system.

B. Inner Loop

The scheme proposed in [22]–[24] is used to control the position of the motors. It includes feedback of the coupling torques Γ_i^{coup}, which makes the dynamics of the controlled

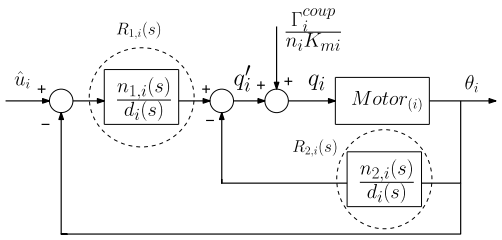

Fig. 2. Inner control loop scheme.

motors insensitive to the movements of the link. This feedback of the coupling torque drastically simplifies the motor models used to design the motor controllers, thus making the design of this inner loop relatively simple.

Let us consider the motor dynamics (6). Fictitious control signals for the motors can, therefore, be defined as $q_i'(t) = q_i(t) - ((\Gamma_i^{\text{coup}}(t))/(n_i K_{mi}))$, which cancel the effect of the link on the motor dynamics by substracting terms proportional to the coupling torques to the real control signals. Moreover, if it were assumed that the Coulomb friction is a step-like disturbance that can be compensated by the loop closed around the motor, the transfer function from the fictitious input to the motor angular position would be obtained as

$$\frac{\theta_i(s)}{q_i'(s)} = G_{mi}(s) = \frac{K_{mi}}{s \cdot (J_i \cdot s + \nu_i)}, \quad i = 1, 2 \tag{7}$$

where $G_{mi}(s)$ is the transfer function between the motor angle $\theta_i(t)$ and the fictitious control signal $q_i'(t)$.

Proportional, integral, and derivative (PID) controllers with a low-pass filter term, i.e., of the form $R(s) = ((a_2 \cdot s^2 + a_1 \cdot s + a_0)/(s \cdot (s + b)))$, ensure good trajectory tracking, compensate disturbances such as unmodeled components of the friction, and are robust to parameter uncertainties, thus providing precise and fast positioning of the motor. These PID controllers are, therefore, used in the inner loop according to the 2-DOF control scheme shown in Fig. 2, in which two of these controllers, $R_{1,i}(s)$ and $R_{2,i}(s)$, are implemented in each motor control in order to place the poles and zeros of the closed-loop system at the desired locations.

The four closed-loop poles of this scheme are placed at the same arbitrary location p_i by following the algebraic method described in [24]. The two zeros of the closed loop are also placed in p_i in order to cancel two poles of the closed loop. The overall transfer functions of the inner loop then become

$$M_i(s) = \frac{\theta_i(s)}{\hat{u}_i(s)} = \frac{1}{(1 + \epsilon_i \cdot s)^2}; \quad \epsilon_i = -p_i^{-1}, \ i = 1, 2 \tag{8}$$

where $\hat{u}_i$ is the command signal for the motor. Since very fast motor movements are desired, the absolute values of poles p_i are high and the values of ϵ_i are, therefore, small.

C. Outer Loop

The system to be controlled by the outer loop is expressed by (1)–(5) plus the two inner loop transfer functions (8). This system has eight states: $\phi_1, \phi_2, \dot{\phi}_1, \dot{\phi}_2, \theta_1, \theta_2, \dot{\theta}_1$, and $\dot{\theta}_2$; two inputs: u_1 and u_2; and two outputs: ϕ_1 and ϕ_2. Moreover, there are four variables that are measured: θ_1, θ_2, Γ_1^{coup}, and Γ_2^{coup}.

Since the model above is nonlinear, the input-state linearization technique (see [5]) is proposed in order to achieve a fast, precise and free-of-vibration outer loop control. Obtaining the controllability and involutivity conditions of this system, along with the linearizing control law, is a highly involved process, yielding very complex mathematical expressions. It is, therefore, difficult to apply to control this system.

An alternative approach was proposed in [21], in which the inner loop dynamics (8) was canceled by adding prefilters to the inputs of the inner loop. These prefilters are of the form $F_i(s) = ((\hat{u}_i(s))/(\hat{u}_i'(s))) = ((1 + \epsilon_i \cdot s)/(1 + \varsigma_i \cdot s))^2$, where $\varsigma_i \ll \epsilon_i$ and $\hat{u}_i'$ are the outputs of the outer loop controller ($i = 1, 2$). These prefilters $F_i(s)$ approximately cancel the inner loop dynamics. The overall system (prefilter-inner loop-link dynamics) can, therefore, be approximated by only the link dynamics (1)–(5).

Since the inner loop dynamics $M_i(s)$ are approximately inverted by prefilters $F_i(s)$, the motor angles $\boldsymbol{\theta}$ closely follow their references $\hat{u}' = (\hat{u}_1' \ \hat{u}_2')^T$, which are generated by the controller of the outer loop, and vector $\boldsymbol{\theta}$ can be substituted for vector $\hat{u}'$ in (1).

Model (1) is not affine in its input $\boldsymbol{\theta}$, signifying that the input-state linearization technique cannot be directly applied. However, it is affine in $\boldsymbol{\mu}$. A fictitious input $\boldsymbol{\mu} = (\mu_1 \ \mu_2)^T$ given by (3) can then be designed [21], which makes (1) affine and allows the implementation of this control technique.

Moreover, some analytical expressions were obtained in [21] that allowed the inversion of the vector field (3), provided that $\boldsymbol{\phi}$ were known. This inversion process is represented as

$$\boldsymbol{\theta} = \boldsymbol{\mu}^{-1}(\boldsymbol{\mu}, \ \boldsymbol{\phi}) \tag{9}$$

and involves the following calculations:

$$\begin{cases} \theta_2 = \arcsin\big(\cos(\phi_2) \cdot \mu_2 \pm \sin(\phi_2) \\ \qquad\qquad \cdot \sqrt{1 - (\mu_1 \cdot \cos(\phi_2))^2 - \mu_2^2}\big) \\ \theta_1 = \phi_1 + \mu_1 \cdot \dfrac{\cos(\phi_2)}{\cos(\theta_2)} \end{cases}. \tag{10}$$

This makes it possible to calculate the real control signal to be provided by the outer loop controller once the fictitious input has been determined. This transformation was used in [21] as the basis on which to successfully implement an input-state linearization controller. However, prefilters $F_i(s)$ are phase-lead compensators that make the actuators prone to saturation when very fast trajectories are demanded.

D. Tip Position Estimator

Tip position can be estimated from the measured variables by equating ϕ_1 and ϕ_2 from (5). The attainment of these angles can be simplified by using the following simple estimator [21]:

$$\phi_1 \approx \theta_1 - \frac{\Gamma_1^{\text{coup}}}{\kappa \cdot \cos(\theta_2)}, \quad \phi_2 \approx \theta_2 - \frac{\Gamma_2^{\text{coup}}}{\kappa} \tag{11}$$

in the most relevant region of the robot workspace.

E. Singularly Perturbed Model

In order to prevent actuator saturations, prefilters $F_i(s)$ of [21] are not used in this article. It rather proposes to use a control system based on a singularly perturbed model in which the inner loop dynamics (8) and the link dynamics (1)–(5) are considered to be the fast and the slow subsystems, respectively. The proposed control combines the inner loop motor control with a state-input feedback linearization of the link dynamics.

1) Open-Loop Dynamic Model: The slow subsystem is modeled by equations (1)–(4). A state model of the fast subsystem (8) can be obtained by defining the state $\hat{\mathbf{z}} = (\boldsymbol{\theta}^T \ \dot{\boldsymbol{\theta}}^T)^T$, the input $\hat{\mathbf{u}} = (\hat{u}_1 \ \hat{u}_2)^T$, $\epsilon = \max(\epsilon_1, \epsilon_2)$, and $\mathbf{A}_z = \text{diag}(\epsilon/\epsilon_1, \ \epsilon/\epsilon_2)$

$$\epsilon \cdot \dot{\hat{\mathbf{z}}} = \mathbf{A} \cdot \hat{\mathbf{z}} + \mathbf{B} \cdot \hat{\mathbf{u}} \tag{12}$$

$$\mathbf{A} = \begin{pmatrix} \mathbf{0}_{2\times 2} & \mathbf{A}_z \\ -\mathbf{A}_z & -2 \cdot \mathbf{A}_z \end{pmatrix}, \quad \mathbf{B} = \begin{pmatrix} \mathbf{0}_{2\times 2} \\ \mathbf{A}_z \end{pmatrix}. \tag{13}$$

2) Reference Trajectory: Let us assume a desired trajectory $\boldsymbol{\phi}^*(t)$ for the robot tip. The corresponding state trajectory should, therefore, be $\hat{\boldsymbol{x}}^*(t) = (\boldsymbol{\phi}^{*T}(t) \ \dot{\boldsymbol{\phi}}^{*T}(t))^T$. Since $(\dot{\hat{x}}_3^*(t) \ \dot{\hat{x}}_4^*(t))^T = \ddot{\boldsymbol{\phi}}^*(t)$, equating $\boldsymbol{\mu}$ in the last two rows of (1) yields

$$\boldsymbol{\mu}^*(t) = K_a^{-1} \cdot (\ddot{\boldsymbol{\phi}}^*(t) - \mathbf{P}(\hat{\mathbf{x}}^*(t))). \tag{14}$$

Once $\boldsymbol{\mu}^*(t)$ has been determined, the desired motor angles $\boldsymbol{\theta}^*(t)$ can be calculated from (9) and (10) as

$$\boldsymbol{\theta}^*(t) = \boldsymbol{\mu}^{-1}\big(K_a^{-1} \cdot (\ddot{\boldsymbol{\phi}}^*(t) - \mathbf{P}(\hat{\mathbf{x}}^*(t))), \boldsymbol{\phi}^*(t)\big). \tag{15}$$

3) Control Law: The input-state feedback linearization technique is used

$$\hat{\mathbf{u}}(t) = \boldsymbol{\mu}^{-1}\big(K_a^{-1} \cdot (\ddot{\boldsymbol{\phi}}^*(t) - \mathbf{v}(t) - \mathbf{P}(\hat{\boldsymbol{x}}(t))), \ \boldsymbol{\phi}^*(t)\big) \tag{16}$$

combined with a linear feedback control law of order n

$$\begin{aligned} \dot{\mathbf{x}}_c(t) &= \mathbf{A}_c \cdot \mathbf{x}_c(t) + \mathbf{B}_c \cdot (\hat{\boldsymbol{x}}(t) - \hat{\boldsymbol{x}}^*(t)) \\ \mathbf{v}(t) &= \mathbf{C}_c \cdot \mathbf{x}_c(t) + \mathbf{D}_c \cdot (\hat{\boldsymbol{x}}(t) - \hat{\boldsymbol{x}}^*(t)) \end{aligned} \tag{17}$$

in which $\mathbf{x}_c \in \Re^{n\times 1}$, $\mathbf{v} \in \Re^{2\times 1}$, $\mathbf{A}_c \in \Re^{n\times n}$, $\mathbf{B}_c \in \Re^{n\times 4}$, $\mathbf{C}_c \in \Re^{2\times n}$, and $\mathbf{D}_c \in \Re^{2\times 4}$. Dynamics (16) and (17) are included in the slow subsystem because they are designed to be much slower than the fast subsystem (12). Model (17) is a generalization of the static feedback control law commonly used in state feedback linearization, which is derived from it by making

$$\mathbf{C}_c = \mathbf{0}, \quad \mathbf{D}_c = \begin{pmatrix} \lambda_1 & 0 & \lambda_3 & 0 \\ 0 & \lambda_2 & 0 & \lambda_4 \end{pmatrix}. \tag{18}$$

4) Closed-Loop Dynamic Model: Define the incremental variables $\boldsymbol{x} = \hat{\boldsymbol{x}} - \hat{\boldsymbol{x}}^*$ and $\mathbf{z} = \hat{\mathbf{z}} - \hat{\mathbf{z}}^*$. Substitute them in the dynamic equations (1)–(3) and (12) and the control law (16) and (17). Operating these equations and combining them yields the incremental dynamic model of $8 + n$ states

$$\begin{aligned} \dot{\mathbf{x}} &= \mathbf{f}(t, \mathbf{x}, \mathbf{z}) \\ \dot{\mathbf{x}}_c &= \mathbf{f}_c(\mathbf{x}, \mathbf{x}_c) \\ \epsilon \cdot \dot{\mathbf{z}} &= \mathbf{g}(t, \mathbf{x}, \mathbf{x}_c, \mathbf{z}). \end{aligned} \tag{19}$$

In this expression, we have that

$$\mathbf{f}(t, \mathbf{x}, \mathbf{z}) = \begin{pmatrix} x_3 \\ x_4 \\ \mathbf{f}_{3,4}(t, \mathbf{x}, \mathbf{z}) \end{pmatrix} \tag{20}$$

where the third and fourth rows of $\mathbf{f}$ are

$$\begin{aligned} &\mathbf{f}_{3,4}(t, \mathbf{x}, \mathbf{z}) \\ &\quad = \mathbf{P}(\mathbf{x} + \hat{\mathbf{x}}^*) - \mathbf{P}(\hat{\mathbf{x}}^*) + K_a \cdot (\boldsymbol{\mu}(\boldsymbol{\theta}, \boldsymbol{\phi}) - \boldsymbol{\mu}(\boldsymbol{\theta}^*, \boldsymbol{\phi}^*)) \end{aligned} \tag{21}$$

where $\boldsymbol{\phi} = \boldsymbol{\phi}^* + \mathbf{C} \cdot \mathbf{x}$ and $\boldsymbol{\theta} = \boldsymbol{\theta}^* + \mathbf{C} \cdot \mathbf{z}$. The dynamics of the control system is

$$\mathbf{f}_c(\mathbf{x}, \mathbf{x}_c) = \mathbf{A}_c \cdot \mathbf{x}_c + \mathbf{B}_c \cdot \boldsymbol{x} \tag{22}$$

and the dynamics of the fast subsystem is

$$\begin{aligned} \mathbf{g}(t, \mathbf{x}, \mathbf{x}_c, \mathbf{z}) = \ &\mathbf{A} \cdot \mathbf{z} - \mathbf{B} \cdot \boldsymbol{\mu}^{-1}\big(K_a^{-1} \cdot (\ddot{\boldsymbol{\phi}}^* - \mathbf{P}(\hat{\mathbf{x}}^*)), \boldsymbol{\phi}^*\big) \\ &+ \mathbf{B} \cdot \boldsymbol{\mu}^{-1}\big(K_a^{-1} \cdot (\ddot{\boldsymbol{\phi}}^* - \mathbf{C}_c \cdot \mathbf{x}_c - \mathbf{D}_c \cdot \mathbf{x} \\ &- \mathbf{P}(\mathbf{x} + \hat{\mathbf{x}}^*)), \boldsymbol{\phi}\big). \end{aligned} \tag{23}$$

It has been assumed that ϵ/ϵ_1 and ϵ/ϵ_2 in $\mathbf{A}_z$ are constant.

F. Stability Analysis of the Closed Loop

The stability of system (19)–(23) is assessed by applying a well-known result of singular perturbation theory (see [5]), which yields the following theorem.

Theorem: Let us consider the system described by (2) and (3), (9) and (10), and (19)–(23), matrices (4) and (13), and trajectories $\hat{\mathbf{x}}^*$ and $\hat{\mathbf{z}}^*$ shown in Section IV-E2 that do not produce vertical configurations ($\hat{x}_2 = \pm\pi/2$ or $\hat{z}_2 = \pm\pi/2$). There consequently exists an $\epsilon^* > 0$, such that for all $\epsilon < \epsilon^*$, the origin of this system is exponentially stable if it is verified that every eigenvalue of matrix

$$\boldsymbol{\Xi} = \begin{pmatrix} \mathbf{0}_{2,2} & \mathbf{I}_2 & \mathbf{0}_{2,n} \\ -\mathbf{D}_{c0} & -\mathbf{D}_{c1} & -\mathbf{C}_c \\ \mathbf{B}_{c0} & \mathbf{B}_{c1} & \mathbf{A}_c \end{pmatrix} \tag{24}$$

has a negative real part. In matrix $\boldsymbol{\Xi}$: $\mathbf{D}_{c0}, \ \mathbf{D}_{c1} \in \Re^{2\times 2}$ are submatrices of $\mathbf{D}_c$, such that $\mathbf{D}_c = (\mathbf{D}_{c0} \ \mathbf{D}_{c1})$, and $\mathbf{B}_{c0}, \ \mathbf{B}_{c1} \in \Re^{nx2}$ are submatrices of $\mathbf{B}_c$, such that $\mathbf{B}_c = (\mathbf{B}_{c0} \ \mathbf{B}_{c1})$.

The proof of this is provided in Appendix I.

Remark 1: The vertical configuration cannot be avoided *a priori*. However, constraints in the desired trajectory can easily be imposed, which prevents the state from reaching that configuration. They are based on the small link deflection assumption cited in Section III-A., which was quantified in [25]; it is verified if the deflection is lower than 10% of the length of the link. Since (12) is the fast subsystem, it is assumed that $\boldsymbol{\theta}(t) \approx \boldsymbol{\theta}^*(t)$ and, hence, $\hat{z}_2(t) \approx \hat{z}_2^*(t)$. The generation of trajectories whose vertical configuration is bounded by $|\hat{z}_2^*(t)| < \pi/2 - 0.1$ consequently guarantees that $|\hat{z}_2(t)| < \pi/2 - 0.1$ and, hence, that $\hat{z}_2(t)$ is not vertical and, therefore, according to the small link deflection condition mentioned that $\hat{x}_2(t)$ would not be either. Note that 0.1 rad $\approx 6°$, which is a small reduction in the robot workspace; attitude movements are permitted between $\pm 84°$ rather than between $\pm 90°$.

Remark 1 imposes that tip trajectories must be designed such that $|\hat{x}_2^*(t)| < \pi/2 - 0.1$. $\hat{z}_2^*(t)$ would subsequently be

obtained from (15) and condition $|\hat{z}_2^*(t)| < \pi/2 - 0.1$ would be checked. If it were not verified, the tip trajectory would have to be modified in order to make $\hat{x}_2^*(t)$ and $\hat{z}_2^*(t)$ simultaneously fulfill the condition given in the remark. Given $\hat{\mathbf{x}}^*(t)$ that verifies the condition, one way of making $\hat{\mathbf{z}}^*(t)$ also verifies it too would be to slow down $\hat{\mathbf{x}}^*$. This would reduce velocities, $\dot{\boldsymbol{\phi}}^*$, and accelerations, $\ddot{\boldsymbol{\phi}}^*$, in (15), which reduces the difference between $\hat{\mathbf{x}}^*$ and $\hat{\mathbf{z}}^*$. Having to perform a task in a vertical configuration is, however, very unlikely, and the robot path through this configuration can be avoided by choosing other intermediate points in order to reach a desired target point.

V. Control System Robust to Strain Gauge Disturbances: Fractional-Order Control

The strain gauges used to measure the moments of the slow subsystem dynamics introduce errors into the estimation of the state $\hat{\mathbf{x}}(t)$ and consequently into the control signal. This section studies how to reduce the effects of these errors in the controlled system. First, a dynamic model of the perturbed system is developed. Conditions are then proposed for the controllers in order to reduce the effects of offset and high-frequency noise. The resulting closed-loop system is subsequently analyzed, and finally, the FOC is designed.

A. Slow Subsystem Model Including Strain Gauge Disturbances

Denote as $\gamma_1(t)$ and $\gamma_2(t)$ the additive errors produced in the measurements provided by the strain gauges of the coupling torques $\Gamma_1^{\text{coup}}(t)$ and $\Gamma_2^{\text{coup}}(t)$. According to (11), the estimate of the tip position is then represented by $\boldsymbol{\phi}_e = \boldsymbol{\phi} + \mathbf{d}$, where

$$\mathbf{d}(t) \approx -\begin{pmatrix} \dfrac{\gamma_1(t)}{\kappa \cdot \cos(\hat{z}_2)} & \dfrac{\gamma_2(t)}{\kappa} \end{pmatrix}^T \tag{25}$$

and the estimate of the slow subsystem state is given by $\hat{\mathbf{x}}_e = \begin{pmatrix} \boldsymbol{\phi}_e^T & \dot{\boldsymbol{\phi}}_e^T \end{pmatrix}^T$. The deviation of this estimate from the reference is $\mathbf{x}_e(t) = \hat{\mathbf{x}}_e(t) - \hat{\mathbf{x}}^*(t)$ or, equivalently

$$\mathbf{x}_e(t) = \mathbf{x}(t) + \boldsymbol{\delta}(t) \tag{26}$$

where $\boldsymbol{\delta}(t) = \begin{pmatrix} \mathbf{d}^T(t) & \dot{\mathbf{d}}^T(t) \end{pmatrix}^T$. Since $\hat{\mathbf{x}}_e(t)$ rather than $\hat{\mathbf{x}}(t)$ is feedback, the dynamics of the controller is

$$\dot{\mathbf{x}}_c = \mathbf{A}_c \cdot \mathbf{x}_c + \mathbf{B}_c \cdot \mathbf{x}_e \tag{27}$$

and the dynamics of the fast subsystem becomes

$$\epsilon \cdot \dot{\mathbf{z}} = \mathbf{A} \cdot \mathbf{z} - \mathbf{B} \cdot \boldsymbol{\mu}^{-1}\left(K_a^{-1} \cdot (\ddot{\boldsymbol{\phi}}^* - \mathbf{P}(\hat{\mathbf{x}}^*)), \boldsymbol{\phi}^*\right) + \mathbf{B} \cdot \hat{\mathbf{u}} \tag{28}$$

$$\hat{\mathbf{u}} = \boldsymbol{\mu}^{-1}\left(K_a^{-1} \cdot (\ddot{\boldsymbol{\phi}}^* - \mathbf{C}_c \cdot \mathbf{x}_c - \mathbf{D}_c \cdot \mathbf{x}_e - \mathbf{P}(\mathbf{x}_e + \hat{\mathbf{x}}^*)), \boldsymbol{\phi}_e\right). \tag{29}$$

Substitute $\mathbf{x}_e$ for (26) and $\boldsymbol{\phi}_e$ by $\boldsymbol{\phi} + \mathbf{d}$ in (29). Assume small values of $\boldsymbol{\delta}$ and $\mathbf{d}$. This makes it possible to approximate (29) using the first term of its expansion in a Taylor series about the real system trajectory $\chi(t) = (\hat{\mathbf{x}}(t),\ \mathbf{x}_c(t),\ \hat{\mathbf{z}}(t))$. This yields the dynamic model of the perturbed slow subsystem

$$\begin{pmatrix} \dot{\mathbf{x}} \\ \dot{\mathbf{x}}_c \end{pmatrix} = \boldsymbol{\Xi} \cdot \begin{pmatrix} \mathbf{x} \\ \mathbf{x}_c \end{pmatrix} + \begin{pmatrix} \mathbf{0}_{2\times 4} \\ -\boldsymbol{\Psi}(\chi) \\ \mathbf{B}_c \end{pmatrix} \cdot \boldsymbol{\delta} \tag{30}$$

where

$$\boldsymbol{\Psi}(\chi) = K_a \cdot \left.\frac{\partial \boldsymbol{\mu}}{\partial \boldsymbol{\phi}}\right|_\chi \cdot \mathbf{C} + \mathbf{D}_c + \left.\frac{\partial \mathbf{P}}{\partial \hat{\mathbf{x}}}\right|_\chi. \tag{31}$$

The Jacobian matrices of this expression are

$$\frac{\partial \boldsymbol{\mu}}{\partial \boldsymbol{\phi}} = \begin{pmatrix} -m_3(\boldsymbol{\theta}, \boldsymbol{\phi}) & m_1(\boldsymbol{\theta}, \boldsymbol{\phi}) \cdot \cos^{-2}(\phi_2) \\ -m_1(\boldsymbol{\theta}, \boldsymbol{\phi}) & -m_2(\boldsymbol{\theta}, \boldsymbol{\phi}) \end{pmatrix} \tag{32}$$

where $m_1(\boldsymbol{\theta}, \boldsymbol{\phi}) = \sin(\theta_1 - \phi_1) \cdot \sin(\phi_2) \cdot \cos(\theta_2)$, $m_2(\boldsymbol{\theta}, \boldsymbol{\phi}) = \sin(\phi_2) \cdot \sin(\theta_2) + \cos(\theta_1 - \phi_1) \cdot \cos(\phi_2) \cdot \cos(\theta_2)$, and $m_3(\boldsymbol{\theta}, \boldsymbol{\phi}) = \cos(\theta_1 - \phi_1) \cdot \cos(\theta_2)/\cos(\phi_2)$, and

$$\frac{\partial \mathbf{P}}{\partial \hat{\mathbf{x}}} = \begin{pmatrix} 0 & \dfrac{2 \cdot \hat{x}_3 \cdot \hat{x}_4}{\cos^2(\hat{x}_2)} & 2 \cdot \tan(\hat{x}_2) \cdot \hat{x}_4 & 2 \cdot \tan(\hat{x}_2) \cdot \hat{x}_3 \\ 0 & m_4(\hat{\mathbf{x}}) & -\sin(2 \cdot \hat{x}_2) \cdot \hat{x}_3 & 0 \end{pmatrix} \tag{33}$$

where $m_4(\hat{\mathbf{x}}) = K_g \cdot \sin(\hat{x}_2) - \cos(2 \cdot \hat{x}_2) \cdot \hat{x}_3^2$. The derivation of this model is detailed in Appendix II.

B. Control Robust to Strain Gauge Offset

Strain gauge offsets are modeled by means of constant disturbances: $\gamma_1(t) = \gamma_{10}$ and $\gamma_2(t) = \gamma_{20}$. The disturbance vector (25) is, therefore

$$\mathbf{d}_0 \approx -\begin{pmatrix} \dfrac{\gamma_{10}}{\kappa \cdot \cos(\hat{z}_{20})} & \dfrac{\gamma_{20}}{\kappa} \end{pmatrix}^T, \quad \boldsymbol{\delta}_0 = \begin{pmatrix} \mathbf{d}_0^T & \mathbf{0}_{1\times 2} \end{pmatrix}^T. \tag{34}$$

This section improves the precision of the tip position by reducing the effect of $\boldsymbol{\delta}_0$ on the steady state of $\hat{\mathbf{x}}$. Steady-state values are represented by $\boldsymbol{\phi}_0$, $\boldsymbol{\theta}_0$, $\hat{\mathbf{x}}_0$, $\mathbf{x}_{c0}$, and $\hat{\mathbf{z}}_0$, their incremental values by $\mathbf{x}_0$ and $\mathbf{z}_0$, and the final state of a reference trajectory by $\hat{\mathbf{x}}_0^*$ and $\hat{\mathbf{z}}_0^*$. Since in the steady state, $\dot{\mathbf{x}} = \mathbf{0}$, $\dot{\mathbf{x}}_c = \mathbf{0}$, and x_3, x_4, δ_3, $\delta_4 = 0$, expression (30) yields

$$\begin{pmatrix} \boldsymbol{\Psi}(\chi) \cdot \mathbf{C}^T \\ -\mathbf{B}_{c0} \end{pmatrix} \cdot \mathbf{d}_0 = \begin{pmatrix} -\mathbf{D}_{c0} & -\mathbf{C}_c \\ \mathbf{B}_{c0} & \mathbf{A}_c \end{pmatrix} \cdot \begin{pmatrix} \mathbf{C} \cdot \mathbf{x}_0 \\ \mathbf{x}_{c0} \end{pmatrix} \tag{35}$$

and eliminating $\mathbf{x}_{c0}$ in this equation gives

$$\left(\mathbf{C}_c \cdot \mathbf{A}_c^{-1} \cdot \mathbf{B}_{c0} - \boldsymbol{\Psi}(\chi) \cdot \mathbf{C}^T\right) \cdot \mathbf{d}_0 = \left(\mathbf{D}_{c0} - \mathbf{C}_c \cdot \mathbf{A}_c^{-1} \cdot \mathbf{B}_{c0}\right) \cdot \mathbf{C}\mathbf{x}_0$$

which shows that, provided that $\mathbf{D}_{c0} - \mathbf{C}_c \cdot \mathbf{A}_c^{-1} \cdot \mathbf{B}_{c0} \neq \mathbf{0}$, the first two states of $\mathbf{x}_0$ are made zero by imposing the condition

$$\mathbf{C}_c \cdot \mathbf{A}_c^{-1} \cdot \mathbf{B}_{c0} - \boldsymbol{\Psi}(\chi) \cdot \mathbf{C}^T = \mathbf{0}. \tag{36}$$

If $\boldsymbol{\Psi}(\chi)$ is substituted for (31), and considering that (32) and (33) are

$$\frac{\partial \boldsymbol{\mu}}{\partial \boldsymbol{\phi}} = \begin{pmatrix} -\dfrac{\cos(\theta_{20})}{\cos(\phi_{20})} & 0 \\ 0 & -\cos(\theta_{20} - \phi_{20}) \end{pmatrix} \tag{37}$$

$$\frac{\partial \mathbf{P}}{\partial \hat{\mathbf{x}}} = \begin{pmatrix} 0 & 0 & 0 & 0 \\ 0 & K_g \cdot \sin(\hat{x}_{20}) & 0 & 0 \end{pmatrix} \tag{38}$$

in the steady state, the following condition is yielded:

$$\mathbf{D}_{c0} - \mathbf{C}_c \cdot \mathbf{A}_c^{-1} \cdot \mathbf{B}_{c0} = K_a \cdot \operatorname{diag}\left(\frac{\cos(\theta_{20})}{\cos(\phi_{20})}, \quad \cos(\theta_{20} - \phi_{20}) - \frac{K_g}{K_a} \cdot \sin(\phi_{20})\right). \tag{39}$$

If $\mathbf{A}_c$, $\mathbf{B}_{c0}$, $\mathbf{C}_c$, and $\mathbf{D}_{c0}$ verify condition (39), the equilibrium point of (30) is $\mathbf{x}_0 = \mathbf{0}$, $\mathbf{x}_{c0} = -\mathbf{A}_c^{-1} \cdot \mathbf{B}_{c0} \cdot \mathbf{d}_0$. In this case, we have that $\hat{\mathbf{x}}_0 = \hat{\mathbf{x}}_0^*$ and $\mathbf{P}(\hat{\mathbf{x}}_0) = \mathbf{P}(\hat{\mathbf{x}}_0^*)$. Moreover, since $\mathbf{f}_{3,4} = \mathbf{0}$, (21) yields that $\boldsymbol{\mu}(\boldsymbol{\theta}_0, \boldsymbol{\phi}_0) = \boldsymbol{\mu}(\boldsymbol{\theta}_0^*, \boldsymbol{\phi}_0^*)$. Considering that $\boldsymbol{\phi}_0 = \boldsymbol{\phi}_0^*$, inverting $\boldsymbol{\mu}$ on the two sides of that equality gives that $\boldsymbol{\theta}_0 = \boldsymbol{\theta}_0^*$. Condition (39) can then be used to tune the controller by substituting the steady state $(\boldsymbol{\phi}_0, \boldsymbol{\theta}_0)$ for the reference steady state $(\boldsymbol{\phi}_0^*, \boldsymbol{\theta}_0^*)$.

Condition (39) imposes constraints in the design of matrix $\mathbf{D}_c$. For example, if the feedback control law commonly utilized in state feedback linearization (18) were used, gains λ_1 and λ_2 would be given by condition (39) and only λ_3 and λ_4 could be tuned to improve the dynamics. Gains λ_3 and λ_4 make it possible to tune only the damping of the closed-loop system and not its speed of response. Alternative control laws must, therefore, be designed in order to simultaneously achieve the desired speed of response and damping while approximately removing the steady-state errors caused by offset.

C. Control Robust to Strain Gauge High-Frequency Noise

Let us consider the state feedback control law (27) with an output equation whose parameters are (18), where state $\mathbf{x}_e(t)$ is corrupted according to (25) and (26). Since signals $\delta_3(t)$ and $\delta_4(t)$ are the time derivatives of $\delta_1(t)$ and $\delta_2(t)$, their amplitudes are high and are amplified by gains λ_3 and λ_4, producing control signals with large high-frequency components that saturate the actuators. The objective of this section is to reduce the effects of this noise on the control signal $\hat{\mathbf{u}}$.

The noise effect can be reduced by canceling the disturbance input matrix in (30), i.e., making $\boldsymbol{\Psi}(\chi) = \mathbf{0}$ and $\mathbf{B}_c = \mathbf{0}$. However, this cannot be achieved by the linear time-invariant controller (17) because: 1) $\boldsymbol{\Psi}(\chi)$ is a time-varying function that, according to (31), cannot be canceled by tuning $\mathbf{D}_c$ and 2) if $\mathbf{B}_c$ were canceled, (17) would be reduced to a gains controller that feeds back the state with gains $\mathbf{D}_c$, which is inconvenient, as stated in the last paragraph of Section V-B. The following approximation is, therefore, proposed.

1) Tune $\mathbf{D}_c$ to the target position at the end of each trajectory. The effect of noise is, therefore, reduced when the robot is motionless. In this case, $\boldsymbol{\Psi}(\chi)$ can be made zero because it is a constant matrix. Applying this condition to (31) and using steady-state reference values (in which $\dot{\boldsymbol{\phi}}_0^* = \dot{\boldsymbol{\theta}}_0^* = \mathbf{0}_{2\times 1}$) yields the tuning laws

$$\mathbf{D}_{c0} = K_a \cdot \begin{pmatrix} m_3(\boldsymbol{\theta}_0^*, \boldsymbol{\phi}_0^*) & -m_1(\boldsymbol{\theta}_0^*, \boldsymbol{\phi}_0^*) \cdot \cos^{-2}(\phi_{20}^*) \\ m_1(\boldsymbol{\theta}_0^*, \boldsymbol{\phi}_0^*) & m_2(\boldsymbol{\theta}_0^*, \boldsymbol{\phi}_0^*) - \dfrac{K_g}{K_a} \cdot \sin(\phi_{20}^*) \end{pmatrix}$$
$$\mathbf{D}_{c1} = \mathbf{0}. \tag{40}$$

2) Since $\dot{\mathbf{d}}(t)$ has a much higher amplitude than $\mathbf{d}(t)$ at high frequencies, the priority is to cancel the input matrix of $\dot{\mathbf{d}}(t)$. We, therefore, propose to make

$$\mathbf{B}_{c1} = \mathbf{0} \tag{41}$$

and $\mathbf{B}_{c0} \neq \mathbf{0}$, and this last matrix is, therefore, the input matrix to the controller.

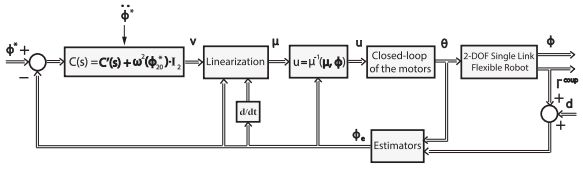

Fig. 3. General control scheme of the system.

The fulfillment of the previous two conditions reduces the effects of $\mathbf{d}$ on $\mathbf{x}$ and $\mathbf{x}_c$. Since these two state vectors are the inputs to the controller output equation of (17), $\mathbf{v}$ is hardly affected by this noise and, hence, the $\mathbf{u}$, $\mathbf{z}$, and $\mathbf{q}$ signals have small noise components.

D. Closed-Loop Analysis

In order to remove the effects of the strain gauge offset and high-frequency noise from the robot steady state, conditions [39]–[41] are imposed on the controller. Substituting $\boldsymbol{\Psi}(\chi) = \mathbf{0}$ in (36) yields that

$$\mathbf{C}_c \cdot \mathbf{A}_c^{-1} \cdot \mathbf{B}_{c0} = \mathbf{0} \tag{42}$$

which, when substituted in (39), gives

$$\mathbf{D}_{c0} = K_a \cdot \operatorname{diag}\left(\frac{\cos(\theta_{20}^*)}{\cos(\phi_{20}^*)}, \quad \cos(\theta_{20}^* - \phi_{20}^*) - \frac{K_g}{K_a} \cdot \sin(\phi_{20}^*) \right). \tag{43}$$

Equations (1)–(4) yield that, in the equilibrium state, $\theta_{10}^* = \phi_{10}^*$ and $\theta_{20}^* = \phi_{20}^* + \arcsin((K_g/K_a) \cdot \cos(\phi_{20}^*))$. Substituting this in (43) and operating gives that

$$K_a \cdot \frac{\cos(\theta_{20}^*)}{\cos(\phi_{20}^*)} = K_a \cdot \cos(\theta_{20}^* - \phi_{20}^*) - K_g \cdot \sin(\phi_{20}^*). \tag{44}$$

Let $\omega^2(\phi_{20}^*)$ denote these two terms. This is expressed as

$$\omega^2(\phi_{20}^*) = \omega_0^2 \cdot \left(\sqrt{1 + (\varpi \cdot \sin(\phi_{20}^*))^2} - \varpi \cdot \sin(\phi_{20}^*)\right) \tag{45}$$

where $\omega_0^2 = (K_a^2 - K_g^2)^{1/2}$ and $\varpi = (K_g/\omega_0^2)$. The 2×2 transfer matrix of controller (17) is, therefore

$$\mathbf{C}(s) = \underbrace{\mathbf{C}_c \cdot (s \cdot \mathbf{I} - \mathbf{A}_c)^{-1} \cdot \mathbf{B}_{c0}}_{\mathbf{C}'(s)} + \underbrace{\omega^2(\phi_{20}^*) \cdot \mathbf{I}_2}_{\mathbf{D}_{c0}} \tag{46}$$

whose input is $\boldsymbol{\phi} - \boldsymbol{\phi}^*$ and whose output is $\mathbf{v}$. Since (42) is verified, $\mathbf{C}'(s)$ is a 2×2 transfer matrix such that $\mathbf{C}'(0) = \mathbf{0}$.

A scheme of the control system with the generic controller (46) is shown in Fig. 3 and will subsequently be analyzed.

Upon applying the Laplace transform to state equation (30), where $\mathbf{B}_{c1} = \mathbf{0}$, $\mathbf{D}_{c1} = \mathbf{0}$ and $\boldsymbol{\Delta}(s)$ denotes the Laplace transform of $\boldsymbol{\Psi}(\chi(t)) \cdot \boldsymbol{\delta}(t)$, we obtain that

$$s^2 \cdot \boldsymbol{\Phi}(s) + \mathbf{C}_c \cdot \mathbf{X}_c(s) + \omega^2(\phi_{20}^*) \cdot \boldsymbol{\Phi}(s) + \boldsymbol{\Delta}(s) = 0$$
$$\mathbf{X}_c(s) = (s \cdot \mathbf{I}_n - \mathbf{A}_c)^{-1} \mathbf{B}_{c0} \cdot (\boldsymbol{\Phi}(s) + \mathbf{D}(s)). \tag{47}$$

Eliminating $\mathbf{X}_c$ in (47) and considering (46) yields that

$$(s^2 \cdot \mathbf{I}_2 + \mathbf{C}'(s) + \omega^2(\phi_{20}^*) \cdot \mathbf{I}_2) \cdot \boldsymbol{\Phi}(s) = -\mathbf{C}'(s) \cdot \mathbf{D}(s) - \boldsymbol{\Delta}(s) \tag{48}$$

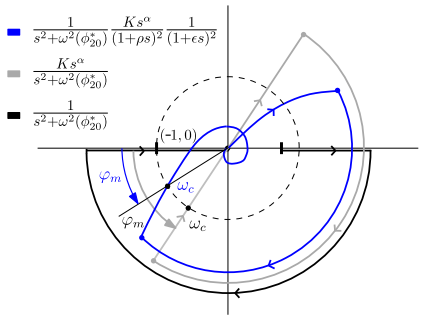

Fig. 4. Nyquist plots of $L(s)$.

whose right-hand side term groups together the disturbances and whose left-hand side term gives the characteristic matricial equation of the closed-loop slow subsystem

$$\mathbf{I}_2 + \mathbf{L}(s) = \mathbf{0}, \quad \mathbf{L}(s) = \frac{1}{s^2 + \omega^2(\phi^*_{20})} \cdot \mathbf{C}'(s). \tag{49}$$

By making $\mathbf{C}'(s) = \text{diag}(C'_1(s),\ C'_2(s))$, (49) is decoupled into two equivalent independent scalar characteristic equations

$$1 + L_i(s) = 0, \quad L_i(s) = \frac{C'_i(s)}{s^2 + \omega^2(\phi^*_{20})}, \quad i = 1, 2. \tag{50}$$

If the same dynamic specifications were imposed on the azimuthal and attitude movements, controllers $C'_i(s)$ could be made equal for the two degrees of freedom.

Expressions (50) show that controllers $C'_i(s)$ have to be tuned before each movement according to the attitude angle ϕ^*_{20} of the target position. Moreover, $\mathbf{D}_{c0}$ in (46) must also be tuned according to ϕ^*_{20}. Methods with which to quickly tune these controllers must, therefore, be developed. This is the objective of Section V-E.

E. Fractional-Order Controller

Let us assume a generic controller $C'(s)$ that can be either $C'_1(s)$ or $C'_2(s)$ and a generic $L(s)$ which is (50) with $C'(s)$. The first path of the Nyquist diagram ($0 < \omega < \infty$) of $L(s)$, assuming that $C'(s) = 1$, i.e., $L(s) = 1/(s^2 + \omega^2(\phi^*_{20}))$, is shown in Fig. 4, and has a marginally stable closed-loop system, i.e., a phase margin $\varphi_m = 0°$. In order to improve the relative stability, i.e., to increase the phase margin, it is necessary to design a phase lead controller $C'(s)$. An obvious strictly proper structure that verifies $C'(0) = 0$ is the real differentiator $C'(s) = K \cdot s/(1 + \rho \cdot s)^\beta$, where $\beta > 1$ is integer and ρ is chosen to be sufficiently small so as to not influence the closed-loop dynamics. However, this structure has only one parameter that can be tuned, K, while at least two parameters have to be tuned in order to simultaneously achieve closed-loop damping and speed of response.

A generalization of the previous structure is proposed here

$$C'(s) = K \cdot \frac{s^\alpha}{(1 + \rho \cdot s)^\beta} \tag{51}$$

where $\alpha > 0$ is a real number. This controller has two parameters to be tuned, K and α, which will be designed using frequency response methods. Expression (51) implements a fractional-order differentiator. The previous real integer-order differentiator is a particular case of (51), making $\alpha = 1$.

Controller (51) cannot be exactly represented by (17). It can, however, be accurately approximated by a state equation or a high-order transfer function. In this case, since (51) is eventually transformed into structure (17), it is possible to propose the use of an IOC of high order rather than an FOC. Methods with which to approximate fractional operators by integer-order models can be found in [18]. This reference provides the algorithms that can increase their accuracy at the cost of increasing the complexity of their integer-order models.

The validity of an approximation depends on the particular application and the control specifications required. This is discussed as follows, in the case of our application. The theorem mentioned in Section IV concerns exponential stability. The only requirements to make the closed-loop system stable with an integer-order approximation of an FOC are, therefore, that: 1) this approximation verifies condition (24) and 2) it is verified that $\epsilon^* > \epsilon$. In addition to stability, two other features have to be considered when assessing the accuracy of this approximation: 1) the error in the phase margin and the gain crossover frequency must be sufficiently small and 2) the fitting error of the frequency response of the FOC achieved by the integer-order approximation must be enough small in the frequency range in which the sensitivity to disturbances is relevant.

We should stress that (51) has the advantage of being much more easily tuned than a high-order IOC (17) because the two parameters of (51) can be tuned in a straightforward manner, the closed-loop frequency response of our system can be more easily interpreted using (51) than using a high-order controller (17), and the phase margin robustness of our system can be easily studied using (51), which would not be the case if an IOC were used. We should also mention that, once the two parameters of (51) have been tuned, the conversion of this controller into an approximate IOC (17) is a simple, almost automatized, process [18]. However, directly tuning all the parameters of a high-order controller (17) in order to obtain a frequency response similar to that achieved by (51) is a complicated and time-consuming process.

Specifications for each $L(s)$ are defined by employing a phase margin φ_m and a gain crossover frequency ω_c, which make it possible to tune closed-loop damping and settling time, respectively. Fig. 4 shows the first path of the Nyquist diagram ($0 < \omega < \infty$) of $L(j \cdot \omega)$ using controller (51) in the case of $\rho = 0$, i.e., $L(s) = K \cdot s^\alpha/(s^2 + \omega^2(\phi^*_{20}))$, in which the corresponding ω_c and φ_m are represented. This diagram shows that the stability of the closed-loop system is ensured if $\omega_c > \omega(\phi^*_{20})$, $\varphi_m > 0$, and $\alpha < 2$. Converting a controller (51) with $\rho = 0$ into one of the form (17) yields an improper controller that violates the conditions stated for high-frequency noise rejection. In what follows, an FOC (51) with $\rho > 0$ will consequently be designed that will aim to reproduce the basic properties highlighted previously.

The following will tune the controller parameters considering the slow linearized dynamics (50) and the fast dynamics (8) jointly. Controllers are then tuned, which verify φ_m and ω_c specifications more accurately than considering the slow

dynamics only. The open-loop transfer function is

$$L(s) = \frac{C'(s)}{\left(s^2 + \omega^2\left(\phi^*_{20}\right)\right) \cdot (1 + \epsilon \cdot s)^2} \tag{52}$$

whose Nyquist plot $L(j \cdot \omega)$ is also shown in Fig. 4.

The tuning of the FOC is carried out by fulfilling the following complex design condition [26]: $L(j \cdot \omega_c) = -e^{j \cdot \varphi_m}$. Equating first phases and then magnitudes in this equation and substituting $(j \cdot \omega_c)^\alpha$ by $\omega_c^\alpha \cdot e^{j \cdot (\pi/2) \cdot \alpha}$ yields that

$$\frac{\pi}{2} \cdot \alpha - \beta \cdot \arctan(\rho \cdot \omega_c) - 2 \cdot \arctan(\epsilon \cdot \omega_c) = \varphi_m \tag{53}$$

and upon equating the magnitudes, we obtain that

$$K = \frac{\left(\omega_c^2 - \omega^2\left(\phi^*_{20}\right)\right)\left(1 + \epsilon^2 \cdot \omega_c^2\right)\left(1 + \rho^2 \omega_c^2\right)^{\frac{\beta}{2}}}{\omega_c^\alpha}. \tag{54}$$

For a given value of ρ, the value of α is easily obtained from (53) and, subsequently, K from (54).

A final step in the design is that of verifying the stability of the closed-loop slow subsystem according to the fourth condition checked in the proof of Theorem (see Appendix I).

VI. Results

In this section, simulations and experiments are carried out in order to prove the advantages of the proposed control technique. Several IOC are compared with our FOC. These controllers are embedded in our nonlinear control scheme, which is robust to sensor disturbances. The standard means of removing sensor offset, based on a high-pass filter, is also assessed.

A. Experimental Setup

The experimental platform is a 2-DOF flexible beam, which is used as a sensing antenna in haptics applications. It has a structure made of stainless steel with three legs to ensure perfect stability. The system is a flexible link, which is attached at one of its ends (denoted as its base) to two dc mini servo actuator PMA-5A motor sets that include harmonic drive reduction gears. These dc motors have incremental optical encoders that measure the angular position of the motors θ_i. The system also has an F-T sensor located at the base of the flexible link that measures torques Γ_i^{coup} at this point. More information about this platform can be found in [24].

Data acquisition and control algorithms are programmed using Labview. Simulations are performed using Simulink/MATLAB. The data acquisition (measurements, control signals, and written data) sampling time is $T_s = 2$ ms.

Tables I and II show the parameters of the two motors and the characteristics of the sensing antenna, respectively, where V_i^{nlc} is the Coulomb friction in terms of voltage.

Fig. 5 shows a photograph of the robotic sensing antenna. It shows a camera-based system, which is used as an external sensor to measure the position of the tip of the flexible link.

B. Identification of the Flexible Link

The dynamics of the link has been identified from its frequency response. A chirp signal in a range of between 0.01 and 50 Hz was used as an input to the azimuthal movement (assuming zero attitude angle) in order to stimulate the vibration modes and obtain the frequency response data of the tip position. This tip position was estimated from the motor position and the coupling torque measurements by using (11). The magnitude and phase of the frequency response are shown in the upper and lower halves of Fig. 6(a), respectively. This figure shows a single vibration mode (a single resonant peak in the magnitude and a single sharp change of 180° in the phase). This experimental result supports the hypotheses of: 1) a massless link with a mass concentrated at its tip and 2) zero rotational inertia at the tip. We note that the angular frequency of the vibration mode of the antenna, 14.6 rad/s, is similar to the theoretical value obtained using the parameters of the antenna $\kappa/(m_t \cdot l^2) = 14.9$ rad/s.

The upper half of Fig. 6(b) shows the signal $\Gamma_1^{\text{coup}}(t)$ provided by the strain gauges when the system is in steady state and the vibration has been removed. This signal should be zero but, instead, has a noticeable disturbance that includes the two unwanted effects: high-frequency noise and offset. The lower half of Fig. 6(b) shows the spectrum of that signal after removing its average value. This shows that significant noise is present in a wide range of frequencies.

TABLE I
Parameters of the Motors

	$K_{mi}(\frac{\text{Nm}}{\text{V}})$	$J_i(\text{Kg} \times \text{m}^2)$	$\nu_i(\text{N} \times \text{m} \times \text{s})$	V_i^{nlc}	n_i
Motor1	0.003	6.2×10^{-3}	30.4×10^{-3}	0.48	100
Motor2	0.003	1.8×10^{-3}	28.5×10^{-3}	0.42	100

TABLE II
Flexible-Link Characteristics

$l(\text{m})$	$m_t(\text{Kg})$	$r(\text{m})$	$\rho'(\text{Kg/m})$	$\kappa(\text{N} \times \text{m})$
0.505	0.01	0.001	4.7×10^{-3}	0.5686

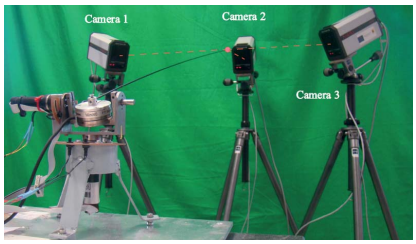

Fig. 5. Photograph of the sensing antenna.

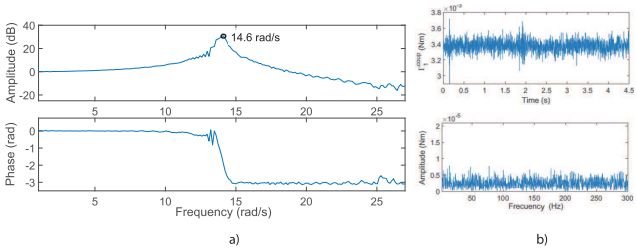

Fig. 6. (a) Identification of the antenna. (b) Sensor disturbance.

C. Specifications of the Control System

The same specifications are imposed on the azimuthal and attitude movements. A single controller $C(s)$ will, therefore, be designed that will be used in the 2-DOF ($C(s) = C_1(s) = C_2(s)$). These specifications are given in the following.

1) The closed-loop system must be robust to motor friction, i.e., it must be insensitive to uncertainties or changes in the Coulomb and viscous friction of the motor. In particular, steady-state errors caused by Coulomb friction must be removed.
2) Frequency specifications $\varphi_m = 70^\circ$ and $\omega_c = 20$ rad/s are tuned in order to achieve the fast and precise tracking of a tip trajectory without exciting the first vibration mode. These specifications were taken from [17].
3) Steady error at the robot tip caused by strain gauges offset must be zero.
4) Effects of the high-frequency noise of the strain gauges must be reduced.

The first specification is achieved by designing the inner loop of the system. Its time constant is set to $\epsilon = 0.017$, i.e., the closed-loop poles at $p = -60$, in the two motors. The PID controllers of the inner loop (using parameters mentioned in Table I) are

$$R_{1,1}(s) = \frac{74.2\ s^2 + 8900s + 2.67 \times 10^5}{s \cdot (s + 235.1)}$$
$$R_{2,1}(s) = \frac{347\ s^2 + 8900s}{s \cdot (s + 235.1)}$$
$$R_{1,2}(s) = \frac{22.2\ s^2 + 2664s + 79.9 \times 10^4}{s \cdot (s + 224.6)}$$
$$R_{2,2}(s) = \frac{89.7\ s^2 + 2664s}{s \cdot (s + 224.6)}.$$

Controllers (46) with a proportional term given by

$$\omega^2 = 222.6 \cdot \left(\sqrt{1 + \left(0.0873 \cdot \sin\left(\phi_{20}^*\right)\right)^2} - 0.0873 \cdot \sin\left(\phi_{20}^*\right)\right) \tag{55}$$

are used in order to achieve the third specification.

D. Simulated Results

Four controllers $C'(s)$ are proposed.

1) *An FOC (51):* A value $\rho = 0.01$ has been chosen as a tradeoff between largely reducing the gain of this controller at high frequencies and hardly degrading the closed-loop performance. Applying the tuning rules (53) and (54) yields controller
$$C'(s) = 2.748 \cdot \frac{s^{1.44}}{(1 + 0.01 \cdot s)^2} \tag{56}$$
which verifies the desired frequency specifications.
2) *An Ideal Derivative Controller $C'(s) = K \cdot s$:* Its only parameter is gain K. This signifies that φ_m and ω_c cannot be simultaneously tuned. The decision was, therefore, made to tune ω_c, which is related to the settling time, resulting in the controller
$$C'(s) = 9.81 \cdot s \tag{57}$$
which has $\omega_c = 20$ rad/s and $\varphi_m = 53.13^\circ$.
3) A real derivative controller that includes a second-order low-pass filter, of the form $C'(s) = K \cdot s/(1 + \rho \cdot s)^2$. As in the previous case, only K can be tuned. Parameter ρ is chosen to be equal to that used in the FOC (56). A controller is, therefore, obtained
$$C'(s) = 10.2 \cdot \frac{s}{(1 + 0.01 \cdot s)^2} \tag{58}$$
with specifications $\omega_c = 20$ rad/s and $\varphi_m = 30.51^\circ$.
4) The previous controller has the required ω_c but needs more phase in order to meet the required phase margin. A phase-lead compensator is, therefore, added to (58) in order to fulfill the φ_m specification. A controller of the form $C'(s) = K \cdot s \cdot (1+\sigma \cdot s)/(1+\rho \cdot s)^\beta$ is consequently proposed, which is the series connection of (58) and a phase-lead term $(1+\sigma \cdot s)/(1+\rho \cdot s)^{\beta-2}$ with $\sigma > \rho$. This term allows us to attain the phase margin specification $\varphi_m = 70^\circ$, in addition to the gain crossover frequency $\omega_c = 20$ rad/s achieved by the previous IOCs. Two parameters now have to be tuned: K and σ. Parameters ρ and β have the sole purpose of guaranteeing the high-frequency noise attenuation conditions (40) and (41). ρ is chosen to be equal to that used in the FOC (56) and the other IOCs, and $\beta = 3$ is chosen in order to make $C'(s)$ strictly proper. A controller is, therefore, obtained
$$C'(s) = 6.6065 \cdot \frac{s \cdot (1 + 0.0613 \cdot s)}{(1 + 0.01 \cdot s)^3} \tag{59}$$
which fulfills the required specifications.

Fig. 7 shows the azimuthal and attitude components of the tip position when the antenna performs a movement with the aforementioned controllers. It shows that the four controllers make the system asymptotically stable and remove the vibration effectively. However, the lowest overshoot is provided by controllers (56) and (59) because their phase margins have been adequately tuned since they are bigger than the phase margins of the other controllers. Moreover, this figure shows that FOC (56) provides slightly more damped responses than (59).

The four previous controllers have been designed using the same gain crossover frequency. However, the phase margins of the controllers are different because we cannot tune the two design specifications with only one parameter in the cases of (57) and (58). One of the advantages of using an FOC is that it allows us to design simpler controllers such as (56), in which the fractional order is used to tune the phase margin. Controller (59) also achieves the two specifications, but its order is higher than that of (56). We could have attempted to retune K and ρ of controller (58) in order to increase its phase margin. However, the simultaneous achievement of φ_m and ω_c implied a negative value of ρ, which would make the closed-loop system unstable. The highest value of the phase margin that can be achieved with this controller is obtained with $\rho = 0$, yielding controller (57). IOCs with two parameters could have been used to tune the two design specifications. However, the condition of eliminating the strain gauge offset $C'(s) = 0$ would have been violated, signifying that only controllers (56) and (59) fulfill the four specifications.

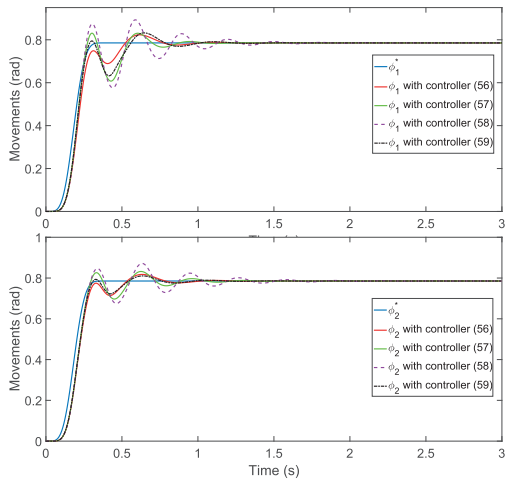

Fig. 7. Components ϕ_1 and ϕ_2 of the tip positioning.

Remark 2: The value of ρ is lower than ϵ. This suggests that part $1/(1+0.01\cdot s)^2$ of the controllers should be included in the fast dynamics subsystem rather than in the slow dynamics subsystem. This can be done by yielding an extended state model (12) that is stable. The fifth condition given in Appendix I is, therefore, verified and, upon repeating the process described in the theorem, the closed-loop stability is also proven in this case.

Finally, we should mention that simulations have been carried out without sensor disturbances because the purpose of this section is to illustrate the superior dynamic performance that can be achieved using our FOC.

E. Sensitivity Analysis of the Slow Subsystem

This section studies the sensitivity functions between the sensor disturbance, $\mathbf{d}(t)$, and the tip angular position, $\boldsymbol{\phi}(t)$, and between $\mathbf{d}(t)$ and the control signal, $\hat{\mathbf{u}}(t) = \boldsymbol{\theta}^*(t)$, which is the reference of the inner loop. This study is carried out for the closed-loop slow subsystem, i.e., it is assumed that $\boldsymbol{\theta}(t) = \boldsymbol{\theta}^*(t)$. The sensitivity functions of controllers (56) and (59), which are the only ones that fulfill the four specifications shown in Section VI-C, are compared here.

The azimuthal and attitude sensitivity functions $S_{\phi_1}(s)$ and $S_{\phi_2}(s)$, between $d_1(t)$ and $\phi_1(t)$, and between $d_2(t)$ and $\phi_2(t)$, respectively, are obtained in Appendix III for the dynamic model linearized around the target position $\boldsymbol{\phi}_0^*$ and $\boldsymbol{\theta}_0^*$. Assuming that $C_1'(s) = C_2'(s) = C'(s)$, expression (80) yields that

$$S_{\phi_1}(s) = \frac{\Phi_1(s)}{D_1(s)} = -\frac{C'(s)}{s^2 + C'(s) + \omega^2\left(\phi_{20}^*\right)} = S_{\phi_2}(s). \quad (60)$$

This sensitivity, which is the same in the 2-DOF, is represented by $S_\phi(s)$.

The azimuthal and attitude sensitivity functions $S_{u_1}(s)$ and $S_{u_2}(s)$, between $d_1(t)$ and $u_1(t)$ and between $d_2(t)$ and $u_2(t)$, respectively, are also obtained in Appendix III for the linearized dynamic model. Signals $u_i(t)$, $i = 1, 2$, are the differences between $\hat{u}_i(t)$ and their values in the target position. Taking (60) and (83) into account yields that

$$S_{u_1}(s) = \frac{U_1(s)}{D_1(s)} = \frac{s^2 + \omega^2\left(\phi_{20}^*\right)}{\omega^2\left(\phi_{20}^*\right)} \cdot S_\phi(s) \quad (61)$$

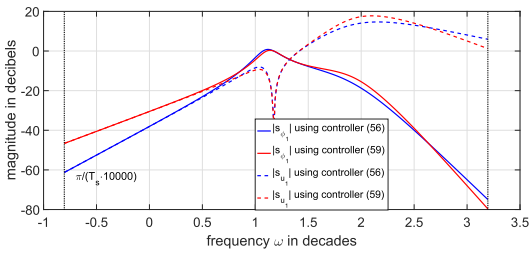

Fig. 8. Sensitivity functions $|S_\phi(j\cdot\omega)|$ and $|S_{u_1}(j\cdot\omega)|$.

$$S_{u_2}(s) = \frac{U_2(s)}{D_2(s)} = \frac{K_a \cdot \cos\left(\theta_{20}^* - \phi_{20}^*\right)}{\omega^2\left(\phi_{20}^*\right)} \cdot S_{u_1}(s). \quad (62)$$

Since (62) shows that $S_{u_2}(s)$ is proportional to $S_{u_1}(s)$, any of these two functions can be used to compare controllers. Moreover, (61) shows that the frequencies at which one controller has a higher sensitivity than the other coincide in $S_\phi(s)$ and $S_{u_1}(s)$ and, because of (62), in $S_{u_2}(s)$.

Fig. 8 shows the magnitudes of $S_\phi(j\cdot\omega)$ and $S_{u_1}(j\cdot\omega)$ yielded by controllers (56) and (59). These functions are represented in a frequency range whose upper limit is the Nyquist frequency π/T_s and whose lower limit is 4 decades below. This figure shows that the following holds.

1) $|S_\phi(j\cdot\omega)|$ and $|S_{u_1}(j\cdot\omega)|$ are lower with controller (56) than with controller (59) in most of the frequency range. Only in the small interval (7.1, 14.9) rad/s (14.9 is $\omega(\phi_{20}^*)$), and at very high frequencies (over 435.5 rad/s), does controller (56) have slightly higher sensitivity than (59).
2) The sensitivity at low frequencies is significantly lower with (56) than with (59). For each of these controllers, $|S_\phi(j\cdot\omega)|$ and $|S_{u_1}(j\cdot\omega)|$ almost coincide at low frequencies. This can easily be seen by substituting $s = j\cdot\omega$ in (61) and then making the limit $\omega \to 0$.
3) The slope of $|S_\phi(j\cdot\omega)|$ and $|S_{u_1}(j\cdot\omega)|$ at low frequencies is 28.8 dB/decade with controller (56) and 20 dB/decade with (59). Low-frequency disturbances are, therefore, rejected by (56) much better than by (59). In fact, while both controllers yield tip position zero steady-state error to step disturbances, controller (56) yields tip position zero steady-state error to ramp disturbances, unlike (59), which yields a constant steady-state error. These last two features can be proved by applying the final value theorem of the Laplace transform to (60).

As a consequence, (56) rejects the disturbances better than (59) at most frequencies, and this feature is significant at low frequencies.

A disturbance in the azimuthal degree of freedom is simulated in order to assess the time behavior of the control system using controllers (56) and (59). Fig. 9 shows the disturbance, $d_1(t)$. It mimics the real disturbance registered and shown in Fig. 6(b). An offset of 0.0034 is suddenly applied at 0 s and, after 4 s, we make this offset grow linearly for 6 s up to a value of 0.045. This offset is then maintained for 4 s. The high-frequency noise shown in Fig. 6 is added to the offset in the entire time interval.

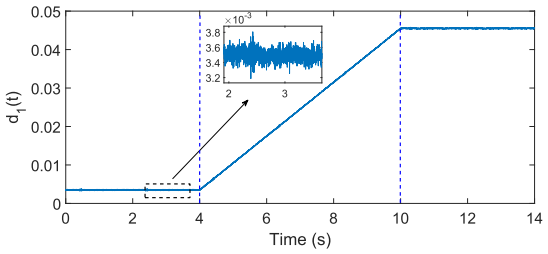

Fig. 9. Disturbance $d_1(t)$ applied to the sensor.

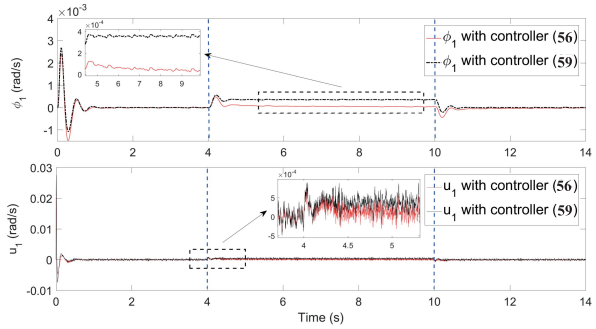

Fig. 10. Simulated results with controllers (56) and (59).

Fig. 10 shows the responses $\phi_1(t)$ and $\hat{u}_1(t)$ to the above disturbance. There is a transient behavior at the beginning caused by a sudden change in the value of the offset from 0 to 0.0034. The upper plots in this figure show that both controllers (56) and (59) efficiently remove the tip position steady-state error caused by the constant offset. However, FOC (56) removes the error caused by the linear variation in the offset, while (59) does not (it yields a steady-state error).

The lower plots in Fig. 10 show that both controllers moderately amplify the sensor high-frequency noise, producing control signals $\hat{u}_1(t)$ that do not saturate the actuators, although the control signal yielded by (56) has a high-frequency noise of slightly less amplitude than that yielded by (59). These simulations validate the results predicted by the previous analysis of the sensitivity functions. Similar results are obtained for the elevation degree of freedom.

F. Simulated Results Using a High-Pass Filter

In this section, a high-pass filter is included in our control scheme in order to remove the offset of the sensor. In this case, condition (39) is not necessary and there is no constraint in the design of matrix $\mathbf{D}_c$. The controllers described in Section IV-E3 are used here, signifying that gains λ_1 to λ_4 can be freely tuned. The high-pass filter removes the dc component of the measured moments. In the steady state, $\Gamma_1^{\text{coup}} = \Gamma_2^{\text{coup}} = 0$ and (11), therefore, yield that $\boldsymbol{\phi}^e = \boldsymbol{\theta}$. Control signal (17) is consequently $\mathbf{v} = \text{diag}(\lambda_1,\ \lambda_2)\cdot(\boldsymbol{\theta} - \boldsymbol{\phi}^*)$. Upon substituting $\mathbf{v}$ in (16) and considering (2), $\hat{\mathbf{u}}$ is obtained. Upon substituting $\hat{\mathbf{u}}$ in (10), considering that $\boldsymbol{\theta}^* = \boldsymbol{\theta}$ in the steady state and operating, the conditions that allow the attainment of the references for the motor angles are yielded

$$\theta_1^* = \phi_1^*; \quad \lambda_2 \cdot \left(\phi_2^* - \theta_2^*\right) + K_g \cdot \cos\left(\theta_2^*\right) = 0. \tag{63}$$

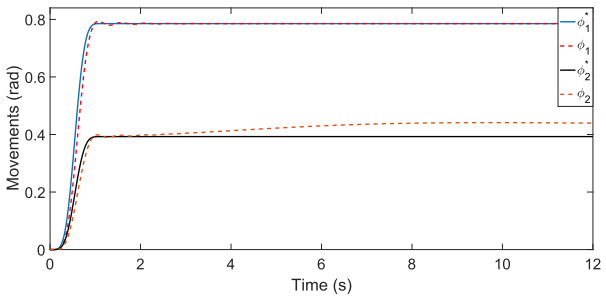

Fig. 11. Component ϕ_1 of tip positioning using filter $H_{h\text{-}p}(s)$.

The fictitious input $\boldsymbol{\mu}$ is obtained from (3) by substituting the real values $\boldsymbol{\phi}$ of the tip position and considering that $\boldsymbol{\theta}^* = \boldsymbol{\theta}$. Upon substituting $\boldsymbol{\mu}$ and the value of (2) in (1), considering the steady-state condition and using the real values $\boldsymbol{\phi}$, the conditions that make it possible to obtain the tip position are yielded

$$\phi_1 = \phi_1^*; \quad K_g \cdot \cos(\phi_2) = K_a \cdot \sin\left(\theta_2^* - \phi_2\right). \tag{64}$$

The error in the component ϕ_1 is, therefore, zero. However, the combination of the right-hand side equations of (63) and (64) (eliminating θ_2^* between these two equations) shows a significant deviation of ϕ_2 with respect to ϕ_2^*.

Simulations were carried out using the control scheme of Fig. 3 and a high-pass filter between the sensor measurement sensor and the estimators. The aforementioned frequency specifications $\varphi_m = 70°$ and $\omega_c = 20$ rad/s were used to tune the controllers. The gains of (18) were $\lambda_1 = \lambda_2 = 136.8$ and $\lambda_3 = \lambda_4 = 18.8$. The high-pass filter was designed by following the procedure explained in [27].

A third-order Butterworth filter (low-pass filter, H_{l-p}) with a cutoff frequency of $\omega_c = 0.5$ rad/s (about 1 decade lower than the gain crossover frequency) was designed and was subsequently transformed into a high-pass filter, $H_{h\text{-}p}$, using the transformation $H_{h\text{-}p}(s) = 1 - H_{l-p}(s)$. It has the form $H_{h\text{-}p}(s) = ((s^3 + s^2 + 0.5s)/(s^3 + s^2 + 0.5s + 0.125))$. Fig. 11 shows the azimuthal and attitude components of the tip position when the antenna performs a 3-D movement. They show that the steady-state tip position error is $e_1 = \phi_1^* - \phi_1 = 0$ and $e_2 = \phi_2^* - \phi_2 = 0.0443$, i.e., a linear error of 22.37 mm. The value of e_2 coincides with the values obtained by solving the right-hand side of (63) and (64).

G. Experimental Results

Experiments have been carried out on the platform described in Section VI-A. The F-T sensor placed at the base of the beam measures the components of the coupling torque, which are feedback by the outer control loop. The camera-based optical tracking system shown in Fig. 5 has a precision of 0.05 mm and is used as an external sensor that measures the real tip position only to verify the effectiveness of the proposed control system (it is not used in the closed-loop control). The reference trajectories are curves formed of fourth-order polynomials designed to meet the needs of driving flexible links [20]. The maneuver was designed that it would neither produce large link deflections nor motor saturation.

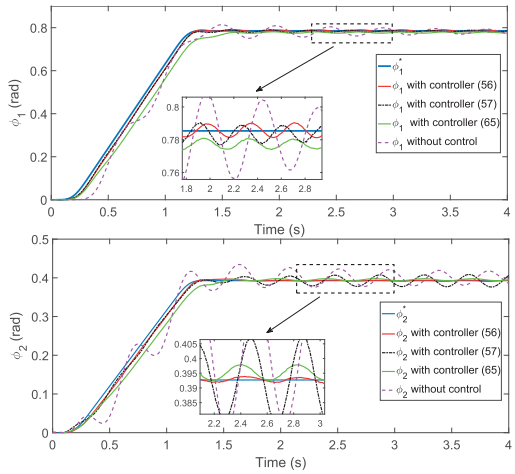

Fig. 12. Component ϕ_1 and ϕ_2 of the tip positioning.

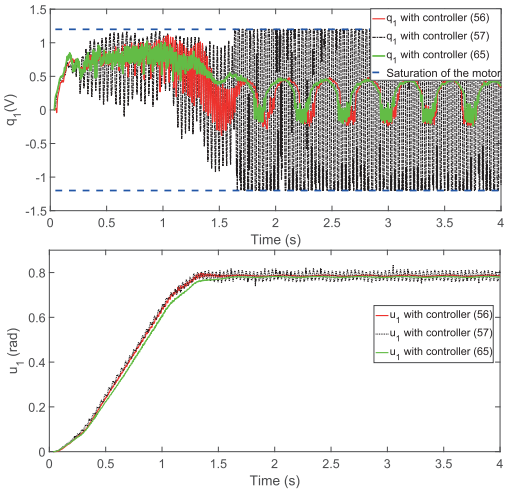

Fig. 13. Control signals and command signals.

This section shows the design of an integer-order PD controller of the form $C'(s) = (K_p + K_v \cdot s)/(1 + \rho \cdot s)^2$. This controller has two gains, K_p and K_v, to be tuned. This, therefore, allows the two frequency specifications ($\omega_c = 20$ rad/s and $\varphi_m = 70°$) to be accomplished, but at the cost of violating the condition $C'(0) = 0$, which is necessary in order to obtain robustness to sensor offset. Using the same ρ as in previous controllers, we obtain that

$$C'(s) = -129.8\frac{1 - 0.0606 \cdot s}{(1 + 0.01 \cdot s)^2}. \tag{65}$$

This controller is used in order to demonstrate the importance of removing the influence of the offset of the sensor in the precise positioning of the antenna. The response of the antenna using the proposed FOC is also compared with controller (57) in order to demonstrate the importance of considering the influence of the high-frequency noise of the sensor. Controller (58) has been discarded because simulations showed an undesirable low damped behavior due to its low phase margin. Complete controllers $C(s)$ are tuned using expression (55) according to the attitude angle ϕ_{20}^* of the target position. For $\phi_{20}^* = \pi/8$, they are $C(s) = C'(s) + 215.25$.

Fig. 12 shows the components of the tip position measured by the camera-based optical tracking system.

Experiments using the scheme in Fig. 3 with the following controllers: are reported: 1) FOC (56); 2) controller (57); 3) PD controller (65); and 4) only motor control. This figure shows that (56) and (65) remove the vibration effectively, although a little residual vibration remains. It also shows that the FOC effectively removes the steady-state error due to the offset of the sensor, whereas the IOC does not. The tip position steady-state error using (65) is 6×10^{-3} rad in each of its components. The offset of the sensor, therefore, produces an error in the steady-state tip position of 5 mm (the distance between the position of the tip and the reference in the steady state). Controller (57) is not able to remove vibrations and the system becomes unstable (the amplitude of ϕ_2 is gradually increasing in Fig. 12).

Fig. 13 shows control signals q_1 and command signals $\hat{u}_1$ of the three controllers and the effect of the high-frequency sensor noise (the other components q_2 and $\hat{u}_2$ are similar and, then, are not shown).

TABLE III
CONTROLLERS

C(s)	(56)	(57)	(58)	(65)	(67)
ω_c	20	20	20	20	20
φ_m	70°	53.13°	30.51°	70°	70°
ω_c'	20.76	20.63	20.62	20.55	20.6
φ_m'	106.9°	90°	67.4°	106.9°	106.47°
ε^*	0.083	0.0455	0.033	0.083	0.0741

The residual vibration shown in Fig. 12, and using (56) and (65), is caused by the high Coulomb friction of the motors (see Table I). The residual vibration in component ϕ_2 (amplitude of 0.2 mm at the tip) is considerably lower than that in ϕ_1 (amplitude of 2 mm at the tip) because the Coulomb friction of Motor 2 is lower than that of Motor 1. Although the inner loop almost removes the effects of nonlinear and time-varying frictions, small errors in the positioning of the motors caused by high Coulomb frictions still remain. These errors are integrated by the integral term of the PID controllers and produce a periodic signal similar to a sawtooth wave (see Fig. 13 for $t > 1.6$ s), which produces this small amount of residual vibration in the positioning of the end-effector. This error is negligible in ϕ_2 but, for the foreseen application, ϕ_1 error is probably not acceptable. It can be reduced by passing the error signal through a static block with a dead zone and lowering the motor controller gains. A methodology with which to design them will be studied in the future.

The effect of high-frequency noise is much higher in controller (57) than in the other two controllers. Moreover, the signal provided by (57) surpasses the saturation limit of the motor, causing the aforementioned instability. Table III shows the frequency specifications achieved with all the controllers designed. In this table, ω_c' and φ_m' are the frequency specifications that would be attained if the fast subsystem dynamics were ignored. Values ϵ^* are also provided, which are the lowest values among the ones obtained after performing

simulations with a set of trajectories that cover all the robot workspace. Since they are higher than our ϵ, the condition required to apply our stability theorem is fulfilled.

H. Implementation of the FOCs

The implementation of FOC (56) used in simulation and experimentation is now outlined. Since $C'(s)$ has been designed in the frequency domain, the method based on fitting the frequency response of the FOC by means of an integer-order transfer function has been chosen. The approximation is carried out in the frequency range $\omega \in [1,\ 300]$ rad/s, which includes the frequency of the vibration mode of the antenna and more than a decade over and below the design frequency ω_c. A third-order transfer function has been fitted to $(j \cdot \omega)^{0.44}$ in the desired range of frequencies using the MATLAB *invfreqs()* function (see [18] for more information about the software packages used to carry out these implementations)

$$\hat{c}(s) = s^{0.44} \simeq \frac{19.6s^3+2636s^2+4.254\times 10^4 s+3.905\times 10^4}{s^3+402.7s^2+1.655\times 10^4 s+6.869\times 10^4} \tag{66}$$

and (56) is approximated by a fifth-order controller

$$C'(s) \simeq 2.748 \cdot \frac{s}{(1+0.01\cdot s)^2} \cdot \hat{c}(s). \tag{67}$$

In order to assess the suitability of approximation (66) and (67) to our application, the issues listed in Section V-E are checked: 1) stability condition (24) is verified; 2) ϵ^* is calculated and it verifies that $\epsilon^* > \epsilon$ (this ϵ^* is very close to that obtained for (56) in Table III); 3) the errors produced by using (67) rather than (56) in the phase margin and the gain crossover frequency are 0.2° and -0.1 rad/s, respectively, which are considered negligible; and 4) the maximum error produced in sensitivity functions (60)–(62) by using (67) rather than (56) is 2 dB, in the frequency range $((\pi/(10\,000\cdot T_s)),\ (\pi/T_s))$ rad/s of Fig. 8, which is regarded as very small. The integer-order approximation is, therefore, considered appropriate.

Remark 3: The FOC is used in the design of the linearized closed-loop system using frequency-domain techniques. However, at the final stage of the design process, it is converted into the approximate IOC of fifth order (66) and (67). Theorem 1, which deals with IOCs of arbitrary order, was subsequently applied using this IOC to verify the stability of the closed-loop system that results with this controller. Consequently, the application of this theorem does not involve any approximation, and the result of the stability analysis is certain.

Remark 4: It is apparent that tuning our FOC and, after, converting it into an approximate IOC using one of the well-established FOC to IOC conversion methods is much easier than directly tuning the fifth-order IOC (66) and (67), which involves tuning at least nine parameters. Moreover, Section VI-E has shown that trying to design an IOC of intermediate complexity like (59) using simple frequency-domain tuning rules would yield a controller that does not reach the disturbance rejection properties achieved by (66) and (67).

VII. Conclusion

This article proposes a two nested loop scheme combined with FOCs in order to account for motor friction and strain gauge disturbances in the control of very lightweight 2-DOF single-link flexible robots.

When provided with a point payload, these robots have only one significant low-frequency vibration mode. Since an inner loop is closed with a high gain controller in order to remove motor friction effects, this dynamics is faster than the link dynamics and prevents the application of the singular perturbation theory to flexible link robots, as has been done in previous research works. This article consequently develops a new control approach that combines state feedback linearization with a singular perturbation method in a different way to that which is usually employed: the motors are considered to be the fast subsystem and the link the slow subsystem.

The main novelty of this article is introducing an FOC in the control system of robotic antennas that outperform the strain gauge disturbance rejection of IOCs. However, another important contribution is condition (39), which allows removing offset sensor disturbances of unknown amplitudes by just tuning adequately the matrix $\mathbf{D}_{c0}$ of the controller. This avoids the use of filters that differentiate the sensor signals ($C'(s)$ has a pure derivative in its numerator, but the complete controller $C(s)$ does not) or controllers that include integral terms that reduce the relative stability of the control system.

The implementation of an FOC often requires its approximation by a high-order IOC. This compelled us to develop a version of the singular perturbation theorem [5] for IOCs of arbitrary order.

Simulations and experiments are reported, which shows that our FOC behaves better than other IOC of similar complexity (only one or two parameters have to be tuned). Our future research will extend this controller to flexible robots with several links.

Appendix I
Proof of Theorem

The conditions of [5, Th. 11.4] are verified in order to prove the stability of the closed-loop system.

By making $\mathbf{x} = \mathbf{x}_c = \mathbf{z} = \mathbf{0}$ in expressions (20)–(23) and operating, the first and second conditions are easily verified.

Making $\mathbf{g}(t, \mathbf{x}, \mathbf{x}_c, \mathbf{z}) = \mathbf{0}$ in expression (23), considering that $\mathbf{A}$ is always invertible and equating $\mathbf{z}$, it yields that

$$\begin{aligned}\mathbf{z} = \mathbf{h}(t,\mathbf{x},\mathbf{x}_c) = \mathbf{A}^{-1}\cdot\mathbf{B}\cdot\boldsymbol{\mu}^{-1}\big(K_a^{-1}\cdot(\ddot{\boldsymbol{\phi}}^* - \mathbf{P}(\hat{\mathbf{x}}^*)), \boldsymbol{\phi}^*\big) \\ - \mathbf{A}^{-1}\cdot\mathbf{B}\cdot\boldsymbol{\mu}^{-1}\big(K_a^{-1}\cdot(\ddot{\boldsymbol{\phi}}^* - \mathbf{C}_c\cdot\mathbf{x}_c - \mathbf{D}_c\cdot\mathbf{x} - \mathbf{P}(\hat{\mathbf{x}}))\boldsymbol{\phi}\big)\end{aligned} \tag{68}$$

which shows isolated roots $\mathbf{z}$. Moreover, it is easy to verify that $\mathbf{h}(t, \mathbf{0}, \mathbf{0}) = \mathbf{0}$. The third condition is, therefore, fulfilled.

The fourth condition is verified next. By making $\epsilon = 0$ in (12), we obtain that $\mathbf{A}\cdot\hat{\mathbf{z}} = -\mathbf{B}\cdot\hat{\mathbf{u}}$, while substituting $\hat{\mathbf{u}}$ for the control law (16) and (17) yields that

$$\hat{\mathbf{z}} = -\mathbf{A}^{-1}\cdot\mathbf{B}\cdot\boldsymbol{\mu}^{-1}\big(K_a^{-1}\cdot(\ddot{\boldsymbol{\phi}}^* - \mathbf{C}_c\cdot\mathbf{x}_c - \mathbf{D}_c\cdot\mathbf{x} - \mathbf{P}(\hat{\mathbf{x}})), \boldsymbol{\phi}\big). \tag{69}$$

Premultiplying both sides of this equation by $\mathbf{C}$ and considering that $-\mathbf{C}\cdot\mathbf{A}^{-1}\cdot\mathbf{B}=\mathbf{I}_2$ gives that

$$\boldsymbol{\theta}=\boldsymbol{\mu}^{-1}\left(K_a^{-1}\cdot(\ddot{\boldsymbol{\phi}}^*-\mathbf{C}_c\cdot\mathbf{x}_c-\mathbf{D}_c\cdot\mathbf{x}-\mathbf{P}(\hat{\mathbf{x}})),\boldsymbol{\phi}\right) \quad (70)$$

A similar relationship is obtained for the reference trajectories

$$\boldsymbol{\theta}^*=\boldsymbol{\mu}^{-1}\left(K_a^{-1}\cdot(\ddot{\boldsymbol{\phi}}^*-\mathbf{P}(\hat{\mathbf{x}}^*)),\boldsymbol{\phi}^*\right) \quad (71)$$

where it has been considered that $\mathbf{x}$ and $\mathbf{x}_c$ are zero when the closed-loop system exactly follows the reference. By substituting (70) and (71) into (21) and considering that $\boldsymbol{\mu}(\boldsymbol{\mu}^{-1}(a,b),b)=a$, $\mathbf{P}(\hat{\mathbf{x}})$ is canceled by $\mathbf{P}(\mathbf{x}+\hat{\mathbf{x}}^*)$ because $\mathbf{x}=\hat{\mathbf{x}}-\hat{\mathbf{x}}^*$ and, operating, gives the dynamics of the reduced system

$$\begin{aligned}\dot{\mathbf{x}}&=\begin{pmatrix}x_3\\x_4\\-\mathbf{C}_c\cdot\mathbf{x}_c-\mathbf{D}_c\cdot\mathbf{x}\end{pmatrix}\\ \dot{\mathbf{x}}_c&=\mathbf{A}_c\cdot\mathbf{x}_c+\mathbf{B}_c\cdot\boldsymbol{x}\end{aligned} \quad (72)$$

which can be expressed as

$$\begin{pmatrix}\dot{\mathbf{x}}\\\dot{\mathbf{x}}_c\end{pmatrix}=\boldsymbol{\Xi}\cdot\begin{pmatrix}\mathbf{x}\\\mathbf{x}_c\end{pmatrix} \quad (73)$$

where $\boldsymbol{\Xi}$ is, therefore, the matrix (24). The origin of the reduced system (73) is, therefore, globally exponentially stable if all the eigenvalues of this matrix have a negative real part. In this case, the fourth condition is verified.

The fulfillment of the fifth condition is verified as follows. Substituting (68) in $\dot{\mathbf{w}}=\mathbf{g}(t,\mathbf{x},\mathbf{x}_c,\mathbf{w}+\mathbf{h}(t,\mathbf{x}))$ and operating easily yields that $\dot{\mathbf{w}}=\mathbf{A}\cdot\mathbf{w}$. Since system (12) is stable, its state matrix $\mathbf{A}/\epsilon$ has all its eigenvalues in the real negative complex half-plane. This signifies that $\mathbf{A}$ is a time-invariant matrix that also has all its eigenvalues in the real negative complex half-plane, and system $\dot{\mathbf{w}}=\mathbf{g}(t,\mathbf{x},\mathbf{x}_c,\mathbf{w}+\mathbf{h}(t,\mathbf{x}))$ is exponentially stable, uniformly in $(t,\mathbf{x},\mathbf{x}_c)$.

Functions $\mathbf{f}$, $\mathbf{g}$, and $\mathbf{h}$ and their derivatives up to order 2 are bounded for $\mathbf{z}-\mathbf{h}(\mathbf{x},t)\in B_\rho$, with the exception of the states in which $\cos(\hat{x}_2)=0$ or $\cos(\hat{z}_2)=0$. These correspond to the vertical configuration of the robot. The sixth condition is, therefore, fulfilled in all the state space, with the exception of the points mentioned in the statement of the theorem.

Appendix II
Derivation of the Perturbed Model of the Slow Subsystem

The first term in the Taylor series expansion of (29) is

$$\hat{\mathbf{u}}\approx\underbrace{\boldsymbol{\mu}^{-1}\left(K_a^{-1}\cdot(\ddot{\boldsymbol{\phi}}^*-\mathbf{C}_c\cdot\mathbf{x}_c-\mathbf{D}_c\cdot\mathbf{x}-\mathbf{P}(\mathbf{x}+\hat{\mathbf{x}}^*)),\boldsymbol{\phi}\right)}_{\hat{\mathbf{u}}_0}+\underbrace{\left.\frac{\partial\hat{\mathbf{u}}}{\partial\mathbf{x}}\right|_\chi\cdot\boldsymbol{\delta}+\left.\frac{\partial\hat{\mathbf{u}}}{\partial\boldsymbol{\phi}}\right|_\chi\cdot\mathbf{d}}_{\boldsymbol{\Delta}\hat{\mathbf{u}}}. \quad (74)$$

The computed inverse of (29) is

$$\begin{aligned}&\boldsymbol{\mu}(\hat{\mathbf{u}}_0+\boldsymbol{\Delta}\hat{\mathbf{u}},\boldsymbol{\phi}+\mathbf{d})\\&\quad\approx K_a^{-1}\cdot(\ddot{\boldsymbol{\phi}}^*-\mathbf{C}_c\cdot\mathbf{x}_c-\mathbf{D}_c\cdot(\mathbf{x}+\boldsymbol{\delta})-\mathbf{P}(\mathbf{x}+\boldsymbol{\delta}+\hat{\mathbf{x}}^*)).\end{aligned} \quad (75)$$

If $\boldsymbol{\Delta}\hat{\mathbf{u}}$, $\mathbf{d}$, and $\boldsymbol{\delta}$ are small when compared to $\hat{\mathbf{u}}_0$, $\boldsymbol{\phi}$, and $\mathbf{x}$, respectively, (75) can be linearized with respect to $\boldsymbol{\Delta}\hat{\mathbf{u}}$, $\mathbf{d}$, and $\boldsymbol{\delta}$ around the trajectory $\chi(t)$, which yields that

$$\left.\frac{\partial\boldsymbol{\mu}}{\partial\hat{\mathbf{u}}_0}\right|_\chi\cdot\boldsymbol{\Delta}\hat{\mathbf{u}}\approx-\left.\frac{\partial\boldsymbol{\mu}}{\partial\boldsymbol{\phi}}\right|_\chi\cdot\mathbf{d}-K_a^{-1}\cdot\left(\mathbf{D}_c+\left.\frac{\partial\mathbf{P}}{\partial\hat{\mathbf{x}}}\right|_\chi\right)\cdot\boldsymbol{\delta}. \quad (76)$$

Making $\epsilon=0$ in (28) and substituting (15) and (74) yields

$$\mathbf{z}=\mathbf{A}^{-1}\cdot\mathbf{B}\cdot(\boldsymbol{\theta}^*-\hat{\mathbf{u}}_0-\boldsymbol{\Delta}\hat{\mathbf{u}}). \quad (77)$$

Note that substituting the differential equation (28) for (77) does not modify the effect of $\mathbf{d}$ on the steady-state error of $\hat{\mathbf{x}}$. However, since (28) acts as a low-pass filter, substituting this for (77) amplifies the effect of the high-frequency components of $\mathbf{d}$ on $\hat{\mathbf{x}}$. A control system designed to attenuate the effects of these high-frequency disturbances in a closed-loop system with the algebraic equation (77) will, therefore, attenuate them better in the original system that has dynamics (28).

Since $-\mathbf{C}\cdot\mathbf{A}^{-1}\cdot\mathbf{B}=\mathbf{I}_2$, (77) can be expressed as $\mathbf{C}\cdot\hat{\mathbf{z}}=\boldsymbol{\theta}=\hat{\mathbf{u}}_0+\boldsymbol{\Delta}\hat{\mathbf{u}}$. Substituting this in (21) and subsequently linearizing $\boldsymbol{\mu}(\hat{\mathbf{u}}_0+\boldsymbol{\Delta}\hat{\mathbf{u}},\boldsymbol{\phi})$ with respect to $\boldsymbol{\Delta}\hat{\mathbf{u}}$ gives that

$$\begin{aligned}\mathbf{f}_{3,4}(t,\mathbf{x},\mathbf{z})\approx\mathbf{P}(\hat{\mathbf{x}})-\mathbf{P}(\hat{\mathbf{x}}^*)+K_a\cdot\boldsymbol{\mu}(\hat{\mathbf{u}}_0,\boldsymbol{\phi})+K_a\cdot\left.\frac{\partial\boldsymbol{\mu}}{\partial\hat{\mathbf{u}}_0}\right|_\chi\\\cdot\boldsymbol{\Delta}\hat{\mathbf{u}}-K_a\cdot\boldsymbol{\mu}(\boldsymbol{\theta}^*,\boldsymbol{\phi}^*).\end{aligned} \quad (78)$$

The inversion of $\hat{\mathbf{u}}_0$ defined in (74) gives $\boldsymbol{\mu}(\hat{\mathbf{u}}_0,\boldsymbol{\phi})=K_a^{-1}\cdot(\ddot{\boldsymbol{\phi}}^*-\mathbf{C}_c\cdot\mathbf{x}_c-\mathbf{D}_c\cdot\mathbf{x}-\mathbf{P}(\hat{\mathbf{x}}))$. The inversion of (15) gives $\boldsymbol{\mu}(\boldsymbol{\theta}^*,\boldsymbol{\phi}^*)=K_a^{-1}\cdot(\ddot{\boldsymbol{\phi}}^*-\mathbf{P}(\hat{\mathbf{x}}^*))$. Substituting these two expressions in (78) and operating yields

$$\mathbf{f}_{3,4}\approx-\mathbf{C}_c\cdot\mathbf{x}_c-\mathbf{D}_c\cdot\mathbf{x}+K_a\cdot\left.\frac{\partial\boldsymbol{\mu}}{\partial\mathbf{u}_0}\right|_\chi\cdot\boldsymbol{\Delta}\hat{\mathbf{u}}. \quad (79)$$

Substituting (76) into (79) and the result in (20), substituting (26) into (27), and combining these results yields the dynamic model of the perturbed slow subsystem.

Appendix III
Obtention of the Sensitivity Function of the Slow Subsystem Between $\mathbf{D}(t)$ and $\boldsymbol{\theta}^*(t)$

Consider (48). According to Section V-C, our control system has been tuned to make $\boldsymbol{\Psi}(\chi)=\mathbf{0}$ in the target position. This implies that $\boldsymbol{\Delta}(s)=\mathbf{0}$. Moreover, let us assume that $\mathbf{C}'(s)$ is diagonal. Equation (48) can, therefore, be split into two scalar equations that yield transfer functions

$$\frac{\Phi_i(s)}{D_i(s)}=-\frac{C_i'(s)}{s^2+C_i'(s)+\omega^2(\phi_{20}^*)},\quad i=1,2. \quad (80)$$

The relationship between $\boldsymbol{\phi}$ and $\boldsymbol{\theta}$ is given by the dynamic nonlinear model (1). Since we are studying the sensitivity to small disturbances $\mathbf{d}(t)$ in the steady state, this equation can be linearized around the target position $\boldsymbol{\phi}_0^*$, $\boldsymbol{\theta}_0^*$, yielding that

$$\dot{\boldsymbol{x}}=\begin{pmatrix}x_3\\x_4\\\dfrac{\partial\mathbf{P}}{\partial\hat{\boldsymbol{x}}}\cdot\boldsymbol{x}+K_a\cdot\dfrac{\partial\boldsymbol{\mu}}{\partial\hat{\boldsymbol{x}}}\cdot\boldsymbol{x}+K_a\cdot\dfrac{\partial\boldsymbol{\mu}}{\partial\hat{\boldsymbol{z}}}\cdot\boldsymbol{z}\end{pmatrix} \quad (81)$$

Jacobian $\partial\mathbf{P}/\partial\hat{\boldsymbol{x}}$ is given by (38), in which $\hat{x}_{20}$ is made equal to ϕ_{20}^*. Jacobian $(\partial\boldsymbol{\mu}/\partial\hat{\boldsymbol{x}})$ is $((\partial\boldsymbol{\mu}/\partial\boldsymbol{\phi})\ \ \mathbf{0}_{2\times2})$, in which

$(\partial \boldsymbol{\mu}/\partial \boldsymbol{\phi})$ is given by (37), and angles ϕ_{20} and θ_{20} are made equal to ϕ_{20}^* and θ_{20}^*, respectively. Considering that $\phi_{10}^* = \theta_{10}^*$ and operating, we obtain that $(\partial \boldsymbol{\mu}/\partial \hat{\boldsymbol{z}}) = -(\partial \boldsymbol{\mu}/\partial \hat{\boldsymbol{x}})$. Substituting all this in (81) and considering (44) and that $K_a \cdot ((\cos(\theta_{20}^*))/(\cos(\phi_{20}^*))) = \omega^2(\phi_{20}^*)$ yields

$$\begin{pmatrix} \ddot{x}_1 \\ \ddot{x}_2 \end{pmatrix} = -\omega^2\left(\phi_{20}^*\right) \cdot \begin{pmatrix} x_1 \\ x_2 \end{pmatrix} + \begin{pmatrix} \omega^2\left(\phi_{20}^*\right) \cdot z_1 \\ K_a \cdot \cos\left(\theta_{20}^* - \phi_{20}^*\right) \cdot z_2 \end{pmatrix} \tag{82}$$

which can be expressed by the transfer functions

$$\frac{X_1(s)}{Z_1(s)} = \frac{\omega^2\left(\phi_{20}^*\right)}{s^2 + \omega^2\left(\phi_{20}^*\right)}, \quad \frac{X_2(s)}{Z_2(s)} = \frac{K_a \cdot \cos\left(\theta_{20}^* - \phi_{20}^*\right)}{s^2 + \omega^2\left(\phi_{20}^*\right)}. \tag{83}$$

Since we are seeking the sensitivity function of a linearized model, variables $\Phi_i(s)$, $i = 1, 2$, can be substituted in (80) for their corresponding incremental values $X_i(s)$, $i = 1, 2$, respectively. Upon combining (80) and (83) and considering only the slow subsystem dynamics, i.e., $Z_i(s) = \Theta_i^*(s) = U_i(s)$, $i = 1, 2$, the sensitivity functions between $D_i(s)$ and $U_i(s)$ are then obtained.

REFERENCES

[1] C. T. Kiang, A. Spowage, and C. K. Yoong, "Review of control and sensor system of flexible manipulator," *J. Intell. Robotic Syst.*, vol. 77, no. 1, pp. 187–213, Jan. 2015.

[2] G. Dubus, O. David, and Y. Measson, "A vision-based method for estimating vibrations of a flexible arm using on-line sinusoidal regression," in *Proc. IEEE Int. Conf. Robot. Automat.*, May 2010, pp. 4068–4075.

[3] L. Bascetta and P. Rocco, "End-point vibration sensing of planar flexible manipulators through visual servoing," *Mechatronics*, vol. 16, nos. 3–4, pp. 221–232, Apr. 2006.

[4] G. Dubus, "On-line estimation of time varying capture delay for vision-based vibration control of flexible manipulators deployed in hostile environments," in *Proc. IEEE/RSJ Int. Conf. Intell. Robots Syst.*, Oct. 2010, pp. 3765–3770.

[5] H. K. Khalil, *Nonlinear Systems*. Upper Saddle River, NJ, USA: Prentice-Hall, 2002.

[6] A. De Luca, P. Lucibello, and A. G. Ulivi, "Inversion techniques for trajectory control of flexible robot arms," *J. Robot. Syst.*, vol. 6, no. 4, pp. 325–344, Aug. 1989.

[7] A. De Luca and B. Siciliano, "Inversion-based nonlinear control of robot arms with flexible links," *J. Guid., Control, Dyn.*, vol. 16, no. 6, pp. 1169–1176, Nov. 1993.

[8] J. C. Cambera and V. Feliu-Batlle, "Input-state feedback linearization control of a single-link flexible robot arm moving under gravity and joint friction," *Robot. Auton. Syst.*, vol. 88, pp. 24–36, Feb. 2017.

[9] V. Feliu, K. S. Rattan, and H. B. Brown, "Control of flexible arms with friction in the joints," *IEEE Trans. Robot. Autom.*, vol. 9, no. 4, pp. 467–475, Aug. 1993.

[10] B. Siciliano, W. Book, and G. Maria, "An integral manifold approach to control of a one link flexible arm," in *Proc. 25th IEEE Conf. Decis. Control*, Dec. 1986, pp. 1131–1134.

[11] M. Moallem, K. Khorasani, and R. V. Patel, "An integral manifold approach for tip-position tracking of flexible multi-link manipulators," *IEEE Trans. Robot. Autom.*, vol. 13, no. 6, pp. 823–837, Dec. 1997.

[12] B. Xu and P. Zhang, "Composite learning sliding mode control of flexible-link manipulator," *Complexity*, vol. 2017, pp. 1–7, 2017.

[13] B. Xu, "Composite learning control of flexible-link manipulator using NN and DOB," *IEEE Trans. Syst., Man, Cybern., Syst.*, vol. 48, no. 11, pp. 1979–1985, Nov. 2018.

[14] T. Zebin and M. Alam, "Modeling and control of a two-link flexible manipulator using fuzzy logic and genetic optimization techniques.," *JCP*, vol. 7, no. 3, pp. 578–585, 2012.

[15] H. Gao, W. He, C. Zhou, and C. Sun, "Neural network control of a two-link flexible robotic manipulator using assumed mode method," *IEEE Trans. Ind. Informat.*, vol. 15, no. 2, pp. 755–765, Feb. 2019.

[16] J. E. Lavín-Delgado, J. E. Solís-Pérez, J. F. Gómez-Aguilar, and R. F. Escobar-Jiménez, "Trajectory tracking control based on non-singular fractional derivatives for the PUMA 560 robot arm," *Multibody Syst. Dyn.*, vol. 50, no. 3, pp. 259–303, Nov. 2020.

[17] D. Feliu-Talegon and V. Feliu-Batlle, "A fractional-order controller for single-link flexible robots robust to sensor disturbances," *IFAC-PapersOnLine*, vol. 50, no. 1, pp. 6043–6048, Jul. 2017.

[18] C. Monje, Y. Chen, B. Vinagre, D. Xue, and V. Feliu, *Fractional-Order Systems and Controls: Fundamentals and Applications* (Communications and Control Engineering Series). London, U.K.: Springer, 2010.

[19] F. Bellezza, L. Lanari, and G. Ulivi, "Exact modeling of the flexible slewing link," in *Proc. IEEE Int. Conf. Robot. Automat.*, May 1990, pp. 734–739.

[20] F. Ramos, V. Feliu, and I. Payo, "Design of trajectories with physical constraints for very lightweight single link flexible arms," *J. Vib. Control*, vol. 14, no. 8, pp. 1091–1110, Aug. 2008.

[21] C. F. Castillo-Berrio and V. Feliu-Batlle, "Vibration-free position control for a two degrees of freedom flexible-beam sensor," *Mechatronics*, vol. 27, pp. 1–12, Apr. 2015.

[22] V. Feliu, E. Pereira, and I. M. Díaz, "Passivity-based control of single-link flexible manipulators using a linear strain feedback," *Mechanism Mach. Theory*, vol. 71, pp. 191–208, Jan. 2014.

[23] D. Feliu-Talegon and V. Feliu-Batlle, "Improving the position control of a two degrees of freedom robotic sensing antenna using fractional-order controllers," *Int. J. Control*, vol. 90, no. 6, pp. 1256–1281, Jun. 2017.

[24] D. Feliu-Talegon, V. Feliu-Batlle, and C. F. Castillo-Berrio, "Motion control of a sensing antenna with a nonlinear input shaping technique," *RIAI*, vol. 13, no. 2, pp. 162–173, 2016.

[25] T. Beléndez, C. Neipp, and A. Beléndez, "Large and small deflections of a cantilever beam," *Eur. J. Phys.*, vol. 23, no. 3, pp. 371–379, May 2002.

[26] V. Feliu-Batlle, "Robust isophase margin control of oscillatory systems with large uncertainties in their parameters: A fractional-order control approach," *Int. J. Robust Nonlinear Control*, vol. 27, no. 12, pp. 2145–2164, Aug. 2017.

[27] M. J. Chapman, D. P. Goodall, and N. C. Steele, *Signal Processing in Electronic Communications: For Engineers and Mathematicians*. Amsterdam, The Netherlands: Elsevier, 1997.